

Investigation of the Quantum Dynamics of Nitrogen-vacancy Center in Diamond at Zero Magnetic Field

MS Thesis

*submitted in partial fulfillment of the requirements
for the award of the dual degree of*

Bachelor of Science - Master of Science

in

PHYSICS

by

JEMISH NALIYAPARA

(18114)



DEPARTMENT OF PHYSICS

INDIAN INSTITUTE OF SCIENCE EDUCATION AND RESEARCH

BHOPAL - 462066

April 2023



भारतीय विज्ञान शिक्षा एवं अनुसंधान संस्थान भोपाल

Indian Institute of Science Education and Research Bhopal

(Estb. by Ministry of Education, Govt. of India)

CERTIFICATE

This is to certify that **Jemish Naliyapara**, BS-MS (Physics), has worked on the project entitled "**Investigation of the Quantum Dynamics of Nitrogen-vacancy Center in Diamond at Zero Magnetic Field**" under my supervision and guidance. The content of this report is original and has not been submitted elsewhere for the award of any academic or professional degree.

April 2023

IISER Bhopal

Dr. Phani Kumar Peddibhotla

Committee Member

Signature

Date

ACADEMIC INTEGRITY AND COPYRIGHT DISCLAIMER

I hereby declare that this thesis is my own work and, to the best of my knowledge, it contains no materials previously published or written by any other person or substantial proportions of material that have been accepted for the award of any other degree or diploma at IISER Bhopal or any other educational institution, except where due acknowledgment is made in the thesis.

I certify that all copyrighted material incorporated into this thesis is in compliance with the Indian Copyright (Amendment) Act, 2012 and that I have received written permission from the copyright owners for my use of their work, which is beyond the scope of the law. I agree to indemnify and save harmless IISER Bhopal from any, and all claims that may be asserted or that may arise from any copyright violation.

April 2023

IISER Bhopal

Jemish Naliyapara

ACKNOWLEDGEMENTS

“I would like to express my gratitude to the individuals who have guided and supported me throughout my thesis project. As I have the opportunity to acknowledge their contributions, I would like to begin by quoting a Sanskrit sloka:

गुरुब्रह्मा गुरुविष्णुः गुरुर्देवो महेश्वरः ।
गुरुः साक्षात् परं ब्रह्म तस्मै श्री गुरवे नमः ॥

meaning “*Guru is Brahma, Guru is Vishnu, Guru is Shankar; The Guru is the real Parabrahma; Greetings to that guru.*” I am eternally grateful to my parents, who have been the first gurus of my life and a constant source of support at every stage of my life. This thesis is dedicated to them.

I am immensely grateful to my second guru and MS supervisor, Dr. Phani Kumar Peddibhotla, for providing me with the opportunity to conduct my thesis research in the Spin Microscopy Lab. Throughout the course of my research, you provided me with continuous support and guidance, and your efforts to enhance my communication skills are greatly appreciated. Your challenging tasks in the lab and thought-provoking questions during course exams were always inspiring and fascinating, encouraging me to delve deeper into my work. It was an absolute pleasure to work for and with you, and I am thankful for the wonderful experience I had under your guidance. Lastly, I would like to express my gratitude to my third guru, *Bhagvan Shri Swaminarayan*, for being a constant source of strength and encouragement throughout my life.

In addition, I would like to extend my gratitude to PhD students of Spin Microscopy Lab, Mr. Shashank Kumar and Mr. Pralekh Dubey, who taught me all the experiments and provided invaluable assistance in my research work. I am also thankful to them for their guidance in my preparation for GATE and NET exams.

I am deeply grateful to my friends Jinam, Ketan, Smit, Shubham, and Kedar for engaging in thought-provoking discussions and sharing wonderful moments with me during our time at IISERB. Finally, I would also like to express my gratitude to all the individuals who have played a role in my personal growth and development.

ABSTRACT

Quantum technology refers to a rapidly developing field of science that aims to harness the principles of quantum mechanics to create new technologies for computation, communication, and sensing. In recent years, there has been significant research on exploring the nitrogen-vacancy (NV) defects in diamond for quantum sensing applications owing to its unique electron spin properties, which include easy spin initialization, manipulation, and readout measurements. The NV center exhibits exceptional sensitivity to magnetic fields. However, this sensitivity of the NV center is constrained by the effective field, a term used to describe the combined influence of local strain fields and electric fields intrinsic to the diamond lattice.

In this thesis, we investigate the quantum dynamics of the NV center at zero magnetic field. Specifically, we conduct comprehensive studies of the influence of the effective field on the energy levels of a single NV center at zero magnetic field. We also investigate previously unexplored areas of high effective field regimes in the PCD sample. Our results reveal a novel observation of mixing of the spin states and the transition imbalance between them. Additionally, we developed a theoretical formalism for the observed transition imbalance in the spectrum. Our investigation includes a demonstration of the selection rules for spin transition using circularly polarized MW fields and the development of a theoretical model to explain the selectivity of the transition in response to the polarized MW field. Moreover, we demonstrate a technique for addressing dark states that arise in the hyperfine spectrum at zero magnetic field using circularly polarized MW fields. We also demonstrated a novel approach to control transitions between the central transitions at zero magnetic field by simultaneously applying the RF and MW fields. Furthermore, we comprehensively study the transition strength dependency on the orientation of the MW field for NV centers in the (100) oriented diamond sample. Using the insights from this study, we propose a novel technique for vector magnetometry that utilizes the rotation of the MW field.

Through our investigations, we aim to advance the understanding of the behaviour and properties of NV centers at zero magnetic field and contribute to the development of more accurate and precise NV center-based sensing technologies.

LIST OF SYMBOLS AND ABBREVIATIONS

Abbreviations

NV	Nitrogen Vacancy
ISC	Intersystem Crossing
ZFS	Zero Field Splitting
ODMR	Optically Detected Magnetic Resonance
CW ODMR	Continuous Wave ODMR
AOM	Acousto Optic Modulator
RF	Radio Frequency
PCB	Printed Circuit Board
MW	Microwave

Operators

$\hat{\mathbf{S}} = (\hat{S}_x, \hat{S}_y, \hat{S}_z)$	Dimensionless S = 1 spin operators
$\hat{\mathbf{I}} = (\hat{I}_x, \hat{I}_y, \hat{I}_z)$	Dimensionless I = 1 nuclear spin operators
$\hat{U}(t)$	Unitary Operator
\hat{H}_0	Ground state fine and hyperfine Hamiltonian
$\hat{H}_{mw}(t)$	Microwave field and magnetic dipole interaction Hamiltonian
$\hat{H}_{RF}(t)$	RF field and magnetic dipole interaction Hamiltonian
$\hat{\boldsymbol{\mu}}$	Magnetic dipole moment operator
\hat{H}_I	Rotating frame Hamiltonian
$ m_s\rangle$	Ground state fine structure state
$ m_s, m_I\rangle$	Ground state hyperfine state
$E_{ i\rangle}$	Eigenenergy of state $ i\rangle$

Diamonds

SCD	Single Crystalline Diamond
PCD	Polycrystalline Diamond
HPHT	High-Pressure High-Temperature

Interacting Fields

$\mathbf{B} = (B_x, B_y, B_z)$	Static magnetic field
$\Pi = (\Pi_x, \Pi_y, \Pi_z)$	Effective field
A_{HF}	Axial hyperfine parameter
D	zero-field splitting
d_{\parallel}, d_{\perp}	Axial and transverse electric field susceptibilities
$M_{x,y,z}$	Spin-strain susceptibilities
$\Pi_{\parallel}, \Pi_{\perp}$	Axial and transverse effective field
θ_{Π}, ϕ_{π}	Polar and azimuthal angle of effective field
$\mathbf{B}_{mw} = (B_{mw,x}, B_{mw,y}, B_{mw,z})$	MW field amplitude
$\mathbf{B}_{mw}(t)$	Time-dependent MW magnetic field

Constants

$\hbar = 6.626 \times 10^{-34}$ J s	Planck's constant
$\gamma_{NV} = \gamma = 28MHz/mT$	Gyromagnetic ratio of NV spin
$g_e = 2.0028$	Isotropic electron g-factor
$\mu_B = 9.274 \times 10^{-24}$ J/T	Bohr magneton
$\mu_N = 5.051 \times 10^{-27}$ J/T	Nuclear magneton

List of Figures

2.1	Atomic and electronic structure of the NV center in diamond.	5
2.2	Energy level diagram with ODMR of NV center at finite magnetic field	8
3.1	Schematic diagram of home-built confocal setup	11
3.2	Schematic diagram of electronics used in our confocal setup	12
3.3	X-Y and X-Z scan of the diamond using confocal setup	13
3.4	Diamond samples in the lab	13
3.5	Continuous wave ODMR spectrum and its pulse sequence	14
3.6	Rabi oscillation and its pulse sequence	15
3.7	Hyperfine ODMR spectrum and pulsed ODMR sequence	16
4.1	Energy level diagram under the influence of the effective field	19
4.2	High-resolution ODMR spectra of a single NV centers at zero magnetic field	22
5.1	Controlled spin transition via linear, σ^+ and σ^- polarized MW field	26
5.2	NV center in lab frame	26
5.3	Simulation and Experiment plot of CW ODMR with σ^+ and σ^- MW field polarization	28
5.4	Pulsed-ODMR spectrum with dark state at zero magnetic field	29
6.1	Energy level diagram of NV center at zero magnetic field with and without RF field.	32
6.2	Simulation and experiment plot of pulsed-ODMR spectrum at zero magnetic field with and without RF field	35

7.1	Four orientations of NV centers in the (100) oriented diamond sample	38
7.2	Simulation plots of transition strength as a function of MW angle (ϕ_{mw}) . . .	44
7.3	Simulation of the ODMR spectrum of an ensemble of NV centers in the presence of a finite magnetic field	46

Contents

Certificate	i
Academic Integrity and Copyright Disclaimer	ii
Acknowledgements	iii
Abstract	iv
List of Symbols and Abbreviations	v
List of Figures	vii
1 Introduction	1
1.1 Scope of this thesis	2
2 Theoretical Background	4
2.1 Structural and electronic properties	4
2.2 Spin and optical properties	6
2.3 Ground state Hamiltonian of NV center	7
2.4 Microwave spin control	8
3 Experimental Techniques	10
3.1 Experimental Setup	10
3.1.1 Instrumentation	10
3.1.2 Confocal scan	12
3.1.3 Diamond samples	13

3.2	Measurement techniques	14
3.2.1	Continuous wave ODMR	14
3.2.2	Rabi oscillation	15
3.2.3	Pulsed ODMR	16
4	High Resolution Spectroscopy at Zero Magnetic Field	17
4.1	Hamiltonian of NV center at zero magnetic field	18
4.1.1	Eigenenergies and Eigenstates	20
4.2	Experimental results of two different effective field regimes	21
4.2.1	Low effective field regime ($\Pi_{\perp} \ll A_{HF} $)	21
4.2.2	High effective field regime ($\Pi_{\perp} \gtrsim A_{HF} $)	21
4.3	Transition Imbalance	22
5	Selective Transitions Using Circular MW Field	25
5.1	Selectivity of spin transitions	26
5.1.1	Experimental Results	28
5.2	Addressing dark state at zero magnetic field using circular MW field	29
6	Control of Inner States Transition using Radio Frequency	31
6.1	Theoretical model	32
6.2	Experimental result	35
7	MW Polarization-Assisted Vector Magnetometry Using Ensemble of NV Centers	37
7.1	Study of spin transition strength as a function of MW polarization angle	39
7.1.1	Four orientations of NV centers	39
7.1.2	MW angle dependent transition strength for each orientation family .	40
7.1.3	Simulation Results	43
7.2	A novel method for vector magnetometry	44
8	Conclusion and Future Outlook	47
8.1	Conclusion	47

8.2	Outlook	49
A	Spin-1 System	50
A.1	Matrices for Spin-1 System	50
A.2	Ground state Hamiltonian of NV center	50
A.3	Hamiltonian of an NV center at zero magnetic field	52
B	Time-Dependent Hamiltonian in Interaction Picture	53
B.1	Derivation of rotating frame Hamiltonian for the linear MW field	53
B.2	Rotating frame Hamiltonian for arbitrary polarized MW field	56
	Bibliography	58

Chapter 1

Introduction

Quantum mechanics is the foundation of modern physics and has revolutionized our understanding of the fundamental nature of matter and its laws. It has led to numerous technological advancements in recent decades. One of the most exciting applications of quantum physics is the development of quantum technologies, such as quantum computing [1], quantum cryptography [2], and quantum sensing [3]. These technologies harness the principles of quantum mechanics to achieve unprecedented levels of accuracy, security, and computational power.

Over the last decade, there has been tremendous progress in the experimental development of quantum sensors. The nitrogen-vacancy (NV) center in diamond is gaining significant attention as a highly versatile and sensitive sensor with remarkable properties. NV centers are point defects in diamond [4] where a substitution nitrogen atom is adjacent to a lattice vacancy. They exhibit excellent sensitivity to magnetic, electric, and stress fields at room temperature [5, 6, 7], making them a promising candidate for various sensing applications. The well-established optical initialization, spin manipulation with long coherence time [8], and readout by its spin-dependent photoluminescence [9] make the NV center amenable to sensing applications.

In conclusion, the nitrogen-vacancy (NV) center in diamond has emerged as a highly versatile and sensitive quantum sensor that holds great potential for various sensing applications. With its excellent sensitivity to magnetic, electric, and stress fields at room temperature, NV center has been applied in fields such as biology [10, 11], geology [12], ma-

terial science [13, 14], condensed matter physics [15], quantum computation, and information processing [16, 17].

1.1 Scope of this thesis

NV centers found in diamonds have the potential for sensing applications, but there are still obstacles that need to be addressed. One such obstacle is the possibility of inaccuracies in estimating the external magnetic field due to the interaction between the NV center and the intrinsic effective field at zero magnetic field. Therefore, it is crucial to have a better understanding of the local charge and stress environment of the NV center in order to engineer its intrinsic properties effectively, particularly for zero-field sensing applications. This thesis focuses on the quantum dynamics of the NV center at zero magnetic field, exploring its characteristics in depth, and presenting the findings of this investigation.

The thesis commences by providing a theoretical explanation of a critical component of the NV center in chapter 2. The essential characteristics of the NV center are discussed in this chapter. Initially, the structural and electronic properties of the NV center are detailed, followed by a description of the spin and optical properties of the NV center. The ground state Hamiltonian of the NV center is subsequently explained, along with the interaction between the magnetic dipole of the electron and the external MW magnetic field, which triggers the spin transition between the states. This chapter is helpful in understanding the theoretical aspect of the NV center.

Chapter 3 of the thesis details the confocal setup we constructed in-house, including its operational mechanisms and the electronics associated with it. All of our experiments employ this confocal setup. In addition, we covered several types of diamond samples and presented their images in this chapter. The choice of diamond sample is dependent on the experimental requirements. Furthermore, we described several measurement techniques utilized in the experiments, such as continuous wave ODMR, pulsed-ODMR measurement, and Rabi oscillation measurement. This chapter is crucial for comprehending the experimental outcomes depicted in subsequent chapters.

Chapter 4 presents a detailed exploration of the NV center's behaviour under the influence of the effective field. We investigated the two regimes of the effective field and their impact on

the NV center. We also discovered the coupling of the outer hyperfine state, a novel finding we reported in our paper [18]. Furthermore, we comprehensively discussed the impact of the effective field on the transition strength when exposed to an arbitrarily polarized MW field in this chapter. The experimental findings presented in this chapter have significant implications for the development of highly sensitive Quantum sensing-based Magnetometers.

Chapter 5 presents an investigation of the selection rule for magnetic dipole transitions using circular MW fields. We thoroughly discussed our theoretical model that can explain the experimental results. Furthermore, we provided a technique for addressing the dark state that appears in the hyperfine spectra of NV centers at zero magnetic field using a circular polarized MW field. Therefore, this chapter is significant in comprehending the selective transition utilizing circular polarized MW fields.

Chapter 6 introduces a new theoretical model that explains how the transition between inner states occurs when a microwave (MW) field and a radiofrequency (RF) field are applied simultaneously at zero magnetic field. The model's predictions are consistent with the experimental results. Additionally, this technique is useful in determining the strength of an external alternating current (AC) magnetic field.

In the following chapter 7, we introduce the novel method for vector magnetometry. We thoroughly discuss the dependence of transition strength on the MW field orientation for the four NV orientations of the (100) oriented diamond sample in this chapter. The results of our theoretical model allow us to determine the lab frame magnetic field vector completely. Additionally, a novel vector magnetometry method is proposed based on our theoretical model, which can be beneficial in magnetic field imaging experiments.

In chapter 8, a concluding summary and future outlook are provided, which encompasses our findings on NV centers at zero magnetic fields, a new theoretical model, and the advancement of techniques presented in this thesis. Additionally, we explore potential avenues for further research in this field and suggest ways to expand upon the research presented in this thesis.

Chapter 2

Theoretical Background

Diamond is a semiconductor material with a wide band gap of 5.5 eV, corresponding to a wavelength of 225 nm in the ultraviolet (UV) region. Although a perfect diamond crystal is expected to be transparent across a broad range of wavelengths, it is known to host more than 100 colour centers within its wide band gap. These colour centers give diamond unique optical properties, which are commonly used to classify diamonds.

One of the well-known nitrogen-related colour centers in diamond is the nitrogen-vacancy (NV) center. The NV center is a point defect that consists of a substitutional nitrogen atom adjacent to a vacancy in the diamond crystal lattice. This defect can be created through various techniques, such as ion implantation [19], high-pressure high-temperature (HPHT) growth [20], chemical vapour deposition (CVD) [21], and neutron or electron irradiation techniques [22, 23]. The purpose of this chapter is to elucidate the basic properties of the NV center in order to better understand the physics of the NV system.

2.1 Structural and electronic properties

The nitrogen-vacancy is a type of point defect in diamond that exhibits paramagnetic behaviour. It has a tetrahedral shape within the diamond's crystal lattice, which is characterized by the C_{3v} symmetry group. The structure of the defect can be described by the orientation of its major and minor axes of symmetry. The major axis of symmetry is oriented along the $\langle 111 \rangle$ direction, which corresponds to the direction that connects the nitrogen and vacancy atoms within the defect (as shown in figure 2.1(a)).

The NV center possesses charge, orbital, and spin degrees of freedom in its electronic structure. Although there are multiple charge states of the NV defect [24], this thesis focuses on the negatively charged NV center (NV^-) [25] due to its highly desirable quantum properties. Thus, we will refer to the negatively charged state of the NV center simply as NV. In this charge state, the NV center contains six electrons, with five originating from the dangling bonds of the nitrogen and carbon atoms, while the sixth electron is captured from an adjacent donor atom [26].

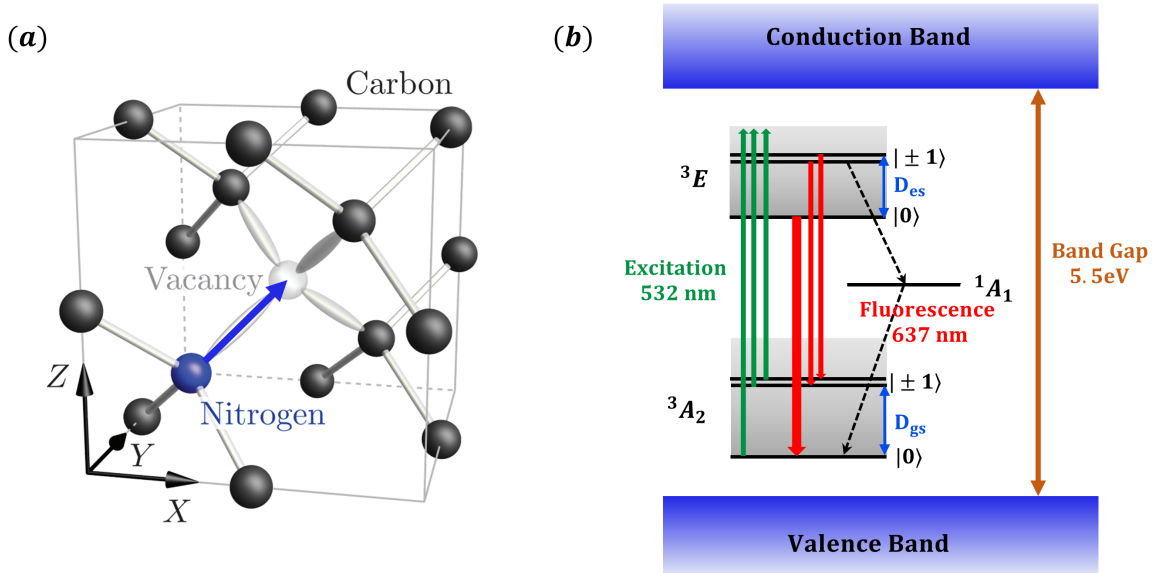


Figure 2.1: (a) NV center is a point defect that occurs within the diamond lattice. It consists of a nitrogen atom (depicted in blue) that has replaced one of the carbon atoms (depicted in black), and a lattice vacancy (shown as transparent space). Its major orientation axis is aligned along the direction that connects the nitrogen atom and the vacancy (blue arrow). (b) NV center energy levels diagram: Green arrows represent the off-resonant optical pumping with a 532 nm (green) laser from the ground state (3A_2) to the excited state (3E). Red arrows represent the fluorescence (637 nm, red); the width of the arrow is qualitatively related to the PL emission rate. Black dashed arrows represent the ISC process through the metastable state (1A_1). The NV center has a ground state zero-field splitting of $D_{gs}=2.87$ GHz and an excited state zero-field splitting of $D_{es}=1.41$ GHz.

The electronic properties of the NV center can be determined using *ab initio* theory, which

has been discussed in [27]. Based on molecular orbital theory, the NV center contains two unpaired electrons, which makes it a spin-1 quantum system. The electronic ground state is a spin-triplet state known as 3A_2 . The NV center can be excited from the ground state 3A_2 to a spin-triplet excited state 3E through an optical dipole transition, as shown in figure 2.1(b). The spin-singlet metastable state is located between the ground and excited state manifolds. All of these states are deeply located within the diamond's bandgap, which is 5.5 eV, so there is no involvement of the valence and conduction bands in the optical transitions. The NV center emits a zero-phonon line at 637 nm [9], accompanied by a vibronic sideband that extends to longer wavelengths.

2.2 Spin and optical properties

In addition to its unique level structure, the NV center presents a fascinating opportunity to use purely optical methods to initialize and read out its ground state spin, as discussed in [9]. The NV defect is characterized as a paramagnetic, S=1 defect that has two unpaired electrons in both its ground and excited states. The states of the NV defect can be described by the eigenstates of the \hat{S}_z operator relative to the NV axis, which is considered as the quantization axis. In the ground state of the NV center, the spin sublevel $|m_s = 0\rangle$ and the degenerate states $|m_s = \pm 1\rangle$ are separated by the zero-field splitting denoted by D. The zero-field splitting arises from the dipolar spin-spin interaction [28]. The splitting between these sublevels is measured to be D = 2.87 GHz.

When a 532 nm laser is used for off-resonant excitation, it can populate states in the vibronic band of the excited state (as indicated by the grey band in figure 2.1(b)) that have a lifetime of around 13 ns [29]. If the spin state initially is in $|m_s = 0\rangle$ and in its ground state (3A_2), it will almost always decay back to the same spin state upon excitation because of spin conservation. On the other hand, if the spin is in the $|m_s = \pm 1\rangle$ state, there are two main possibilities. In approximately 70% of cases, the excited state will decay back to the ground state (3A_2) without changing its spin state. Furthermore, in the remaining roughly 30% of the excited state, the excited state will primarily decay to the intermediate state (1A_1) via a non-spin-conserving, non-radiative decay path, also known as “Intersystem crossing (ISC)” (see figure 2.1(b)). This property allows us to distinguish between the $|m_s = \pm 1\rangle$ states and

the $|m_s = 0\rangle$ state. The $|m_s = \pm 1\rangle$ states exhibit up to $\approx 30\%$ less fluorescence compared to the $|m_s = 0\rangle$ state. The external microwave (MW) fields can be used to drive the spin transition from $|m_s = 0\rangle$ to $|m_s = \pm 1\rangle$. Hence, the spin-dependent fluorescence of the NV center allows us to read out these states via optical pumping and continuous MW frequency sweeping, which is a technique known as optically detected magnetic resonance (ODMR). We will discuss more ODMR techniques in the next chapter.

2.3 Ground state Hamiltonian of NV center

The nitrogen-vacancy center directly interacts with its surrounding environment via dipole-dipole interaction [30]. The Hamiltonian describes to the interaction between the electron spin and different fields, including magnetic field, hyperfine interaction, and local electric field interaction. The spin-1 system can be described by Pauli's spin-1 matrices (see appendix A.1). We consider the NV axis as a quantization axis and the ground triplet states are represented by the eigenstates of \hat{S}_z . The two unpaired electrons interact with each other via spin-spin interaction. Thus, this interaction split the degenerate state $|\pm 1\rangle$ from $|0\rangle$ by zero-field splitting, $D = 2.87$ GHz [9].

These electron spins also interact with the nuclear spins of the surrounding nitrogen and carbon atoms. The hyperfine interaction affects the fine structure levels, leading to the emergence of hyperfine structure. Nitrogen has two stable isotopes, ^{14}N and ^{15}N with nuclear spin of $I=1$ and $I=1/2$, respectively. This nuclear spin creates a local magnetic field surrounding to NV center, causing the splitting of fine structure sublevels into hyperfine sublevels. ^{14}N with nuclear spin, $I=1$, splits each fine structure states into three hyperfine sublevels by hyperfine axial parameter, $A_{HF} = -2.18$ MHz, as depicted in figure 2.2(a). While ^{12}C has a natural abundance of 98.9%, with zero nuclear spin ($I=0$), does not affect the fine structure of the NV center. Isotopic impurities of ^{13}C are randomly distributed within the diamond lattice with a natural abundance of 1.1%. The presence of nuclear spins, specifically the nuclear spin $I = 1/2$ of ^{13}C and ^{15}N , introduces an additional hyperfine interaction that affects the energy levels of the NV spin.

One of the fundamental steps in studying quantum sensing using NV centers is to investigate the Zeeman effect. The Zeeman effect is a phenomenon where the energy levels

of an atom or a molecule are split when it is exposed to a magnetic field. The presence of an external magnetic field induces the Zeeman effect, causing degenerate states $|\pm 1\rangle$ to split into two sublevels $|1\rangle$ and $| - 1\rangle$ with a separation of $2\gamma B$ (See figure 2.2(a)). Here, B represents the magnitude of the projection component of an external magnetic field along the NV axis, and the gyromagnetic ratio of the NV center's electrons is $\gamma = 28$ MHz/mT. The magnitude of the splitting depends on the strength of the magnetic field and the orientation of the NV center relative to the field direction. Calculations for eigenenergies for ground state Hamiltonian are given in Appendix A.2. The splitting can be observed through ODMR spectroscopic technique as data shown in figure 2.2(b). Thus the magnitude of the applied magnetic field can be found using the NV center, hence making it a second-generation magnetometer sensing device. The magnetic field of the order of a few nanoteslas has been sensed by applying much more sensitive techniques [31].

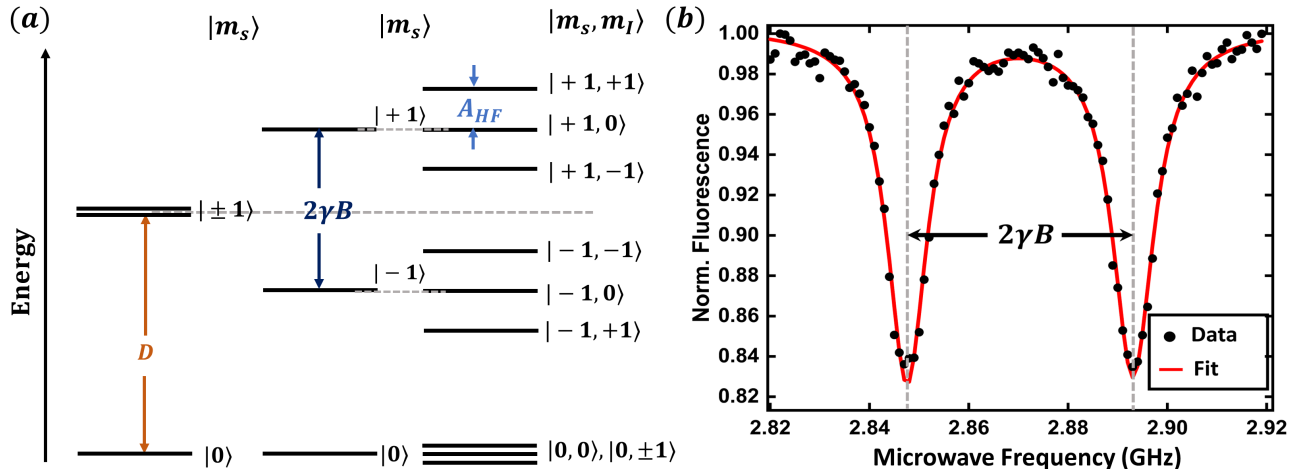


Figure 2.2: (a) Ground state energy level diagram of NV center in the diamond. States $|m_s\rangle$ and $|m_s, m_I\rangle$ on the top line represent the basis of energy level states. (b) ODMR spectrum of a single NV center at a finite magnetic field.

2.4 Microwave spin control

As discussed in the previous section, The Hamiltonian of ground state NV center can be described as,

$$\hat{H} = D\hat{S}_z^2 + A_{HF}\hat{S}_z\hat{I}_z + \gamma\mathbf{B}\cdot\hat{\mathbf{S}} \quad (2.4.1)$$

where $D = 2.87$ GHz is the zero-field splitting (ZFS), $A_{HF} = -2.14$ MHz is the axial hyperfine coupling parameter, $\hat{\mathbf{I}} = (\hat{I}_x, \hat{I}_y, \hat{I}_z)$ is the nuclear spin-1 vector operator of the host ^{14}N spin, $\hat{\mathbf{S}} = (\hat{S}_x, \hat{S}_y, \hat{S}_z)$ is the NV electronic spin-1 operator. We consider $\hbar = 1$ throughout this thesis.

The magnetic dipoles of the NV center interact with the external electromagnetic field to change the NV's spin states in its ground state. The microwave (MW) magnetic field $\mathbf{B}(t) = \mathbf{B}_{mw} \cos(\omega_{mw}t)$ coupled with the magnetic dipole of NV center, and drives the spin transitions. This can be expressed as a time-dependent Hamiltonian,

$$\hat{H}_{mw}(t) = -\mathbf{B}(t) \cdot \hat{\mu} \quad (2.4.2)$$

where $\hat{\mu} = -2\mu_B \hat{\mathbf{S}} = -\gamma \hat{\mathbf{S}}$ is the magnetic dipole operator. This Hamiltonian is responsible for driving the transition from initial state $|i\rangle$ to final state $|f\rangle$. We can calculate the transition probability (or transition strength) using the following formula,

$$P_{|i\rangle \rightarrow |f\rangle} \approx \left| \langle f | \hat{H}_I | i \rangle \right|^2 \quad (2.4.3)$$

Here, \hat{H}_I stands for Hamiltonian in the interaction picture using the rotating frame method as discussed in Appendix B. The interaction picture is a mathematical technique used to simplify the analysis of quantum systems that are subject to time-dependent perturbations. We can simplify the time-dependent Hamiltonian in equation (2.4.2) by applying the rotation operator with MW frequency ω_{mw} and rotating wave approximation (RWA). A thorough discussion about the interaction picture and its application to find transition strength is given in Appendix B. Theoretical descriptions of NV centers helps us to understand and interpret the experimental results.

Chapter 3

Experimental Techniques

3.1 Experimental Setup

NV centers are point defects, so it is important to use a microscopy technique with a high resolution to probe the energy levels. Confocal microscopy helps to illuminate and collect fluorescence from a single NV center. In this section, we will describe how our in-house constructed confocal setup works and the electronic components necessary for its operation. Apart from this, we also discussed the various type of diamonds being used in the lab.

3.1.1 Instrumentation

As shown in figure 3.1, Our confocal setup employs a 532 nm laser beam that is directed through an Acousto Optic Modulator (AOM), which uses a piezo-electric crystal to diffract the laser based on the applied RF frequencies. By modulating the RF frequency, the laser beam can be modulated, and the iris mechanism is used to create pulses and control the laser. The laser beam then passes through a single-mode fibre to reduce the multi-mode laser component into a single-mode Gaussian laser beam. The fibre outputs a collimated laser beam that is sent through a dichroic mirror, with the green light being directed towards the objective lens that focuses the beam on the diamond sample (see figure 3.1). A green laser beam shines on the NV center in the diamond, and it emits red fluorescence in all directions. A small portion of emitted fluorescence is capture by the objective lens and travels back through the same path as the green laser beam. After passing through the dichroic mirror,

it is filtered using a pinhole and converging lens to eliminate background noise. The beam is then returned to its original size using another lens and is finally measured by a single photon counting module (SPCM) or avalanche photon diode (APD).

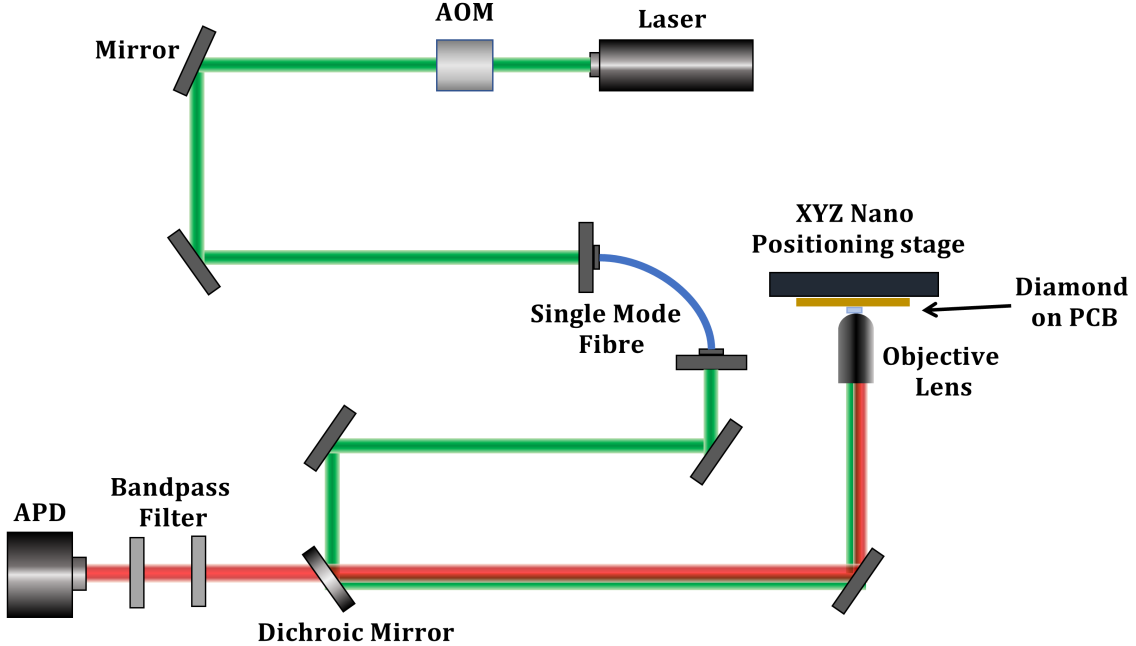


Figure 3.1: Schematic diagram of our home-built confocal setup.

In our confocal setup, the diamond sample is positioned on a nanopositioning system while the objective lens remains fixed. The nanopositioning system is situated on a micropositioning system that allows manual adjustment of the sample position. An oil immersion objective lens is used to collect maximum fluorescence. To create microwave (MW) fields, a 20-micron copper wire is placed on the diamond sample, and MW signals are generated using a signal generator (Keysight). The MW signals are then passed through a MW switch, and an amplifier is used to amplify the output signal. Additionally, a MW switch is inserted between the RF generator and the AOM to modulate the laser pulses in a similar fashion. These MW switches are controlled by digital signals received at the TTL (Transistor-Transistor Logic) terminal. To synchronize the manipulation of the system and the collection of data from the SPCM or APD, a pulse generator (Pulseblaster ESR pro) generates pulse sequences that are fed to the two MW switches and a TimeTagger from Swabian Instruments, which provides time-resolved fluorescence data. All of the electronic components used in the setup

are illustrated in figure 3.2. To control the nanopositioning system and perform the confocal scan, we used Qudi software in a PyCharm environment, while the PulseBlaster ESR Pro was operated via its own graphical user interface. The remaining instruments were controlled using LabVIEW software.

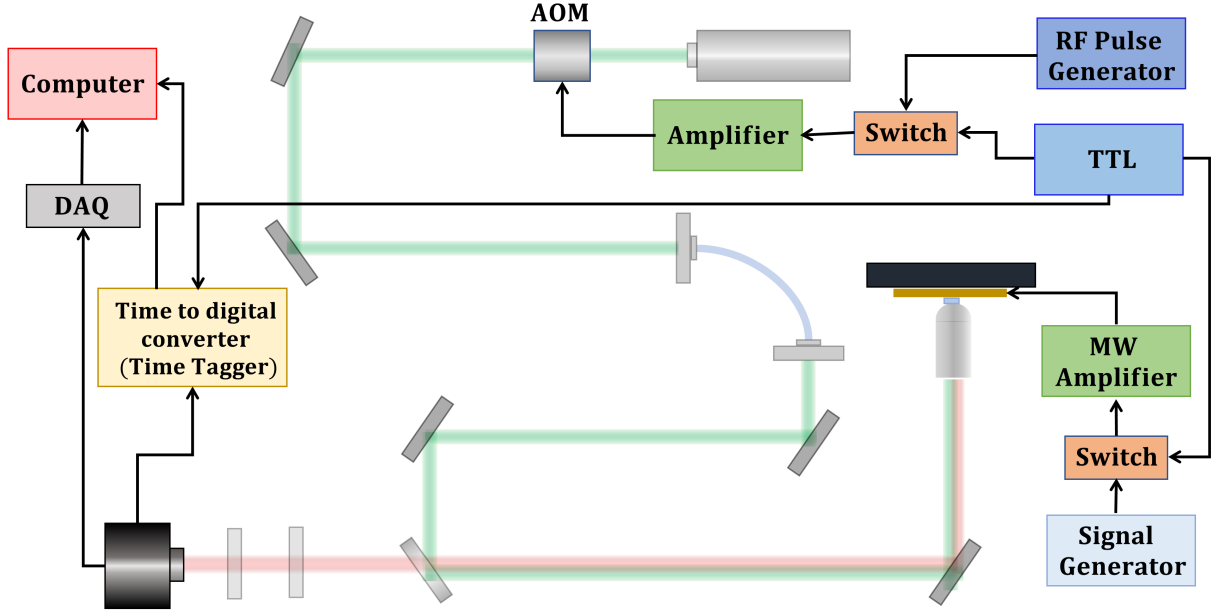


Figure 3.2: Schematic diagram of used electronics to run our confocal setup.

3.1.2 Confocal scan

The confocal scan of the diamond is displayed in figure 3.3, which was obtained using our home-built confocal setup. The Qudi software was used to generate the scanned image by analyzing the data collected by either the APD or SPCM. To collect this data, the APD or SPCM counts the number of photons emitted by the diamond per pixel in a specific area using a raster scanning process aided by a nano-positioning system. Moreover, an X-Z scan can be employed to conduct a depth scan, as shown in figure 3.3(b), where the surface of the diamond appears as a bright horizontal line. An X-Y scan can be performed for surface area scanning, as presented in figure 3.3(a). Each bright orange spot visible in the image represents the NV centers in the diamond. We carried out the experiment by focusing on one of these NV centers.

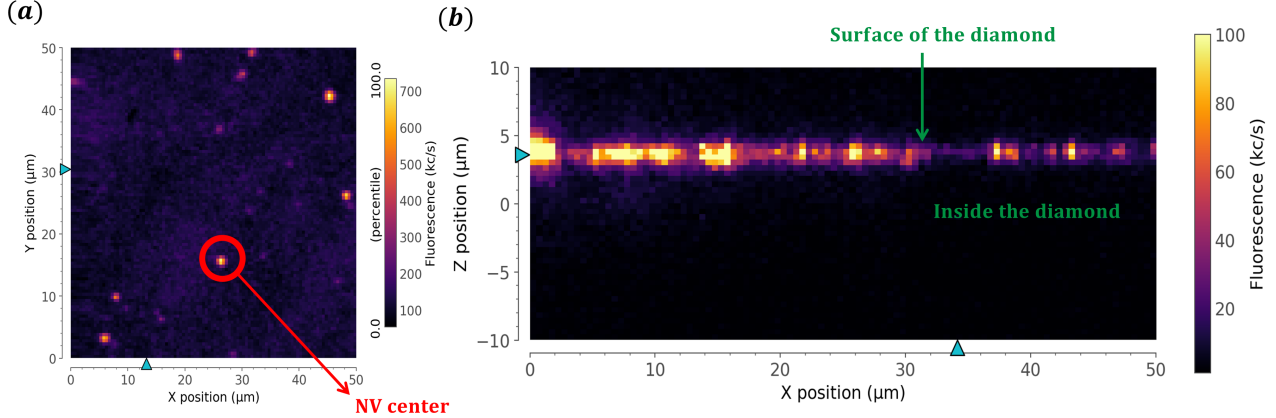


Figure 3.3: (a) X-Y $50\mu\text{m} \times 50\mu\text{m}$ confocal scan. Each bright spots in the scan are NV centers in the diamond. (b) X-Z $20\mu\text{m} \times 50\mu\text{m}$ confocal scan. Surface of the diamond can be seen as bright horizontal line in the scan.

3.1.3 Diamond samples

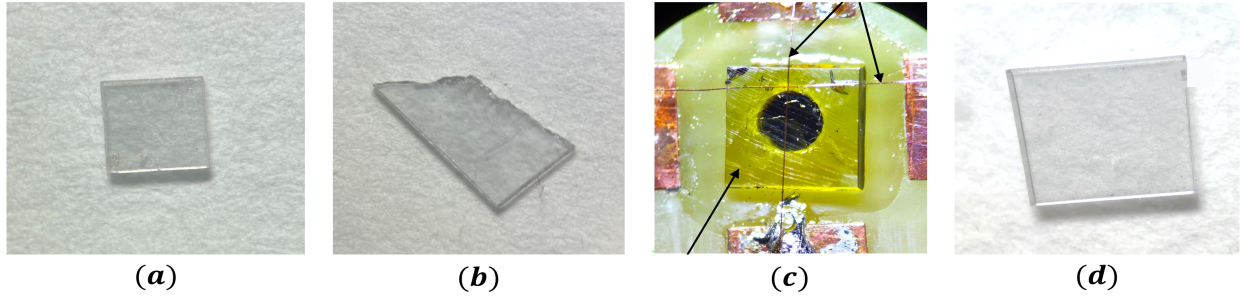


Figure 3.4: (a) $4\text{mm} \times 4\text{mm} \times 0.5\text{mm}$ SCD samples (b) 0.5mm thick PCD sample (c) $3\text{mm} \times 3\text{mm} \times 0.7\text{mm}$ HPHT sample (d) Diamond with ensemble of NV centers

We used different types of diamonds in our lab (see figure 3.4) to investigate NV centers with varying environmental conditions. For observing NV centers in a stress-free environment, we used single-crystalline diamonds (SCD). On the other hand, poly-crystalline diamonds (PCD) were utilized to probe NV centers in a highly stressed environment, which are typically located near grain boundaries in the diamond. We also utilized High-Pressure High-Temperature (HPHT) diamonds, which contain a high concentration of charges in the vicinity of NV centers. Moreover, we employed diamond sample shown in figure 3.4(d) that

contains ensembles of NV centers with a layer of high NV center concentration. These samples were utilized in a variety of experiments, such as stress and strain sensing, charge sensing measurements, and vector magnetometry.

3.2 Measurement techniques

The second section of this chapter covers the techniques that were employed to investigate the energy level structure of the ground state of the NV center, which was discussed in the previous chapter. It is crucial to comprehend these techniques in order to gain a better understanding of the topic.

3.2.1 Continuous wave ODMR

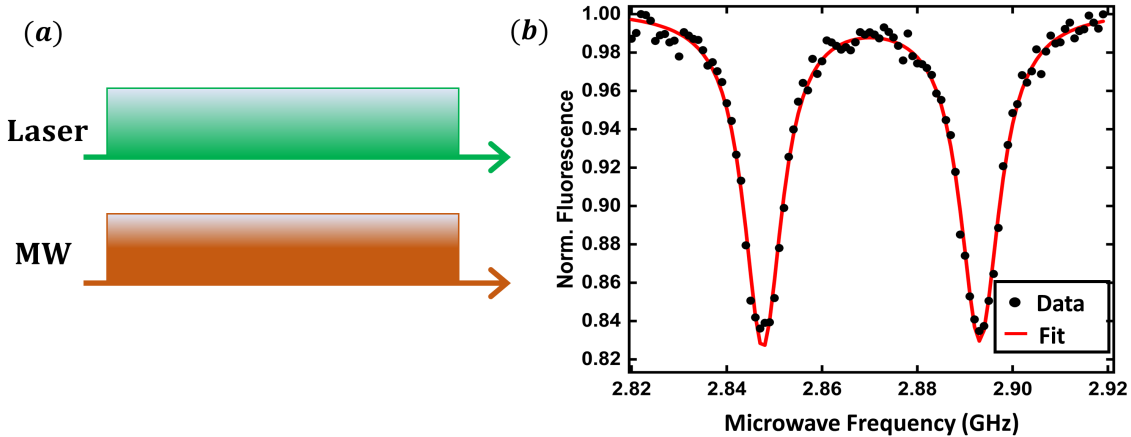


Figure 3.5: (a) Pulse sequence of CW ODMR. (b) ODMR spectrum obtained using CW pulse sequence at a finite magnetic field.

The continuous wave (CW) ODMR technique is a fundamental and crucial experimental method used to investigate the energy levels of NV centers. The fluorescence emitted by the NV center is reliant on its spin state, allowing us to probe its energy levels using its optical property described in Section 2.2. To perform this technique, we continuously shine a green laser beam on the NV center while sweeping the MW frequency as the pulse sequence depicted in figure 3.5(a). The green laser beam continuously excites the electron spin states, and we collect the emitted fluorescence using APD. When the MW frequency matches the energy difference between the spin states, a dip in the fluorescence is observed due to ISC

for $|+1\rangle$ and $| -1\rangle$ states. The complete explanation of ISC is provided in Section 2.2. The CW ODMR spectrum of a single NV at a finite field is shown in figure 3.5(b). Performing CW ODMR spectroscopy on a single NV center allows us to determine the magnitude of the external magnetic field.

3.2.2 Rabi oscillation

One of the important advantages of NV centers is their ability to undergo coherent manipulation of their population. This means that by applying external MW fields with appropriate frequencies and phases, one can control the probability of finding the spin state of the NV center in a specific energy state. When a MW field with resonance frequency is applied to an NV center, the spin state of the NV center oscillates between the $|0\rangle$ and $|+1\rangle$ (or $| -1\rangle$) states. This oscillation is known as Rabi oscillation. The Rabi oscillation experiment involves following the pulse sequence depicted in figure 3.6(a). Initially, the state $|0\rangle$ is prepared using a laser pulse. Next, an MW pulse with a resonance frequency is applied. Finally, the population of the spin state in $|0\rangle$ is measured using a laser beam. The collected fluorescence is then plotted as a function of the MW pulse duration (τ) as shown in figure 3.6(b). The use of Rabi oscillation enables the determination of the T_π time duration for a given MW power, which is particularly useful in high-resolution techniques. The T_π is referred to as the time required to transfer all populations from one spin state to another spin state. Thus, Rabi oscillation measurement helps us to generate π -pulse in the lab.

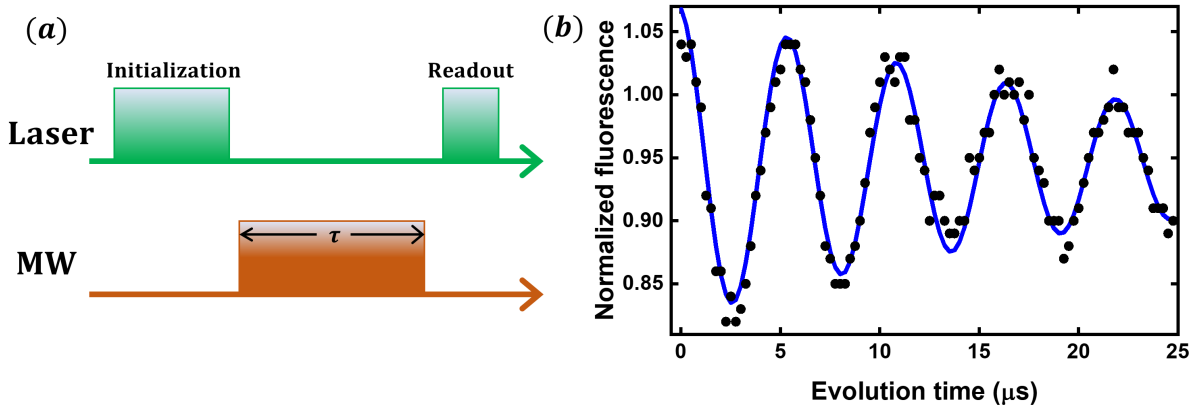


Figure 3.6: (a) Pulse sequence of Rabi oscillation measurement (b) Experimental data of Rabi oscillation.

3.2.3 Pulsed ODMR

The hyperfine structure cannot be resolved in a CW ODMR spectrum due to its broader linewidth (see figure 3.5(b)). In order to overcome this issue and resolve the hyperfine structure of NV centers, Dréau et al. conducted a comprehensive investigation, as presented in [32], and recommend to use of a suitable pulse sequence of the laser beam and microwave pulse to decrease the linewidth. To achieve high-resolution spectroscopy, we employed a combination of laser beam pulse with a duration of 300 ns and MW pulse with a T_π duration, as illustrated in figure 3.7(a). The T_π duration was determined using Rabi oscillation, which was discussed in a previous section. Additionally, we selected the 300 ns duration for the laser pulse as it was found to provide the highest contrast, as shown in [32]. Figure 3.7(b) represents experimental data of the hyperfine structure of a single NV center using this pulse ODMR technique. We also find hyperfine axial parameters from this ODMR spectrum. The pulsed ODMR technique is very useful in various studies like stress and strain sensing at zero magnetic field.

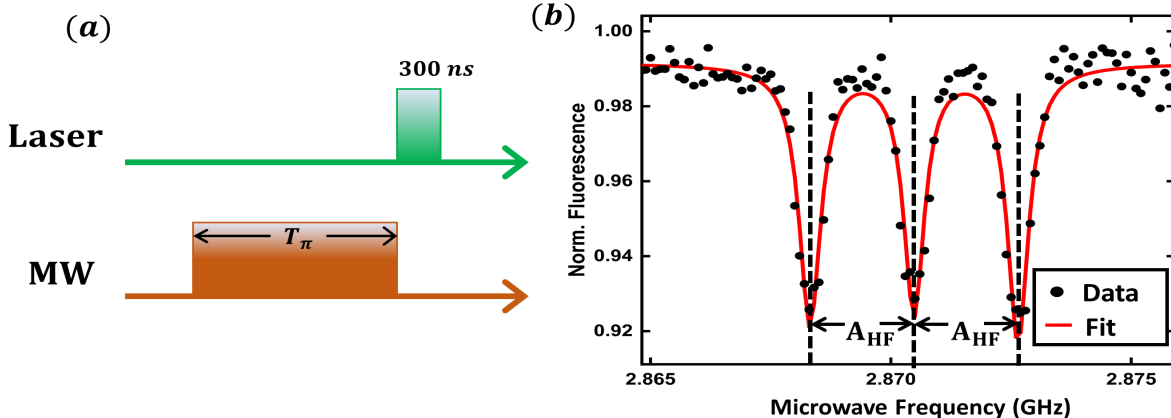


Figure 3.7: (a) Pulse sequence of pulsed ODMR technique (b) ODMR spectrum of hyperfine state of a single NV center at finite field using pulsed ODMR technique.

Furthermore, in our lab, we conducted Ramsey measurements and spin-echo (or Hahn-echo) measurements to determine the T_1 and T_{2^*} relaxation time of the NV center. However, we did not elaborate on these techniques as they were beyond the scope of this thesis.

Chapter 4

High Resolution Spectroscopy at Zero Magnetic Field

One of the most promising applications of NV centers is in quantum sensing, where the ability of the electrons to interact with the environment makes them highly sensitive to external magnetic and electric fields, temperature, and pressure. The remarkable sensitivity of the NV center is both a strength and a weakness. While it allows for the detection of external signals of interest, the NV spin can also be affected by local intrinsic fields from various sources, such as lattice strain, impurities, and surface charges. Techniques like low-field magnetometry [33] and zero-field NMR [34] are susceptible to these intrinsic fields, which can limit the NV's ability to detect and evaluate external signals, especially in low magnetic fields. As a result, more research is needed to precisely understand and characterise the environment surrounding NV spins in order to improve their capabilities and reliability for future applications. This chapter details our investigation into the impact of strain fields and electric fields, collectively referred to as effective fields, on the hyperfine level structure of NV centers. To accomplish this, we utilized high-resolution spectroscopy (pulsed-ODMR measurements) to analyze individual NV centers within a poly-crystalline diamond (PCD) sample.

Previous research on NV centers in PCD samples has demonstrated that they have long coherence times for their ground state electron spin [35], indicating their potential for use in wide-field quantum sensing [36] and quantum information processing [37]. To measure

hyperfine resolved spin transitions of an NV center experiencing a significant intrinsic effective field, we utilized pulsed-ODMR measurements by exploiting the long-lived ground state spin coherence (detailed in Section 3.2.3).

4.1 Hamiltonian of NV center at zero magnetic field

The effective field arising from lattice strain and the electric field induced by surface charge are masked at finite magnetic fields. These fields have an effect on the electronic structure of the NV defect, which is primarily dominated at zero magnetic field. We define the effective field as the combination of both the strain field and the electric field. At zero magnetic field, the spin states $|\pm 1\rangle$ are degenerate. However, the effective field impacts the orbital state of the NV's electrons, leading to a coupling between the hyperfine spin states $|\pm 1, 0\rangle$ due to Spin-Orbital or L-S coupling. As a result of the effective field, the entire spectrum shifts away from the zero-field splitting of ~ 2.87 GHz, and the coupled states split, as shown in figure 4.1(b). Kölbel [38] has suggested that the axial component of the effective field is responsible for the shifting of the spectrum, while the splitting of the inner and/or outer transitions is caused by the transverse component of the effective field.

The Hamiltonian of the NV center \hat{H} , taking into account the intrinsic effective field and axial hyperfine field at zero magnetic field, can be written as [39]:

$$\hat{H} = D\hat{S}_z^2 + A_{HF}\hat{S}_z\hat{I}_z + \Pi_{\parallel}\hat{S}_z^2 + \Pi_x \left(\hat{S}_x^2 - \hat{S}_y^2 \right) + \Pi_y \left(\hat{S}_x\hat{S}_y + \hat{S}_y\hat{S}_x \right) \quad (4.1.1)$$

The system being considered is an NV center, which consists of an electronic spin-1 and a nuclear spin-1 of a ^{14}N nucleus. The Hamiltonian of the system includes terms that arise from the zero-field splitting of the electronic spin and the axial hyperfine coupling between the electronic and nuclear spins. The effective magnetic field acting on the electronic spin is described by the effective field vector $\boldsymbol{\Pi} = (\Pi_x, \Pi_y, \Pi_{\parallel})$, which is expressed in the NV coordinate frame (x, y, z). NV axis is along the z-axis, and the x-axis lies in one of the symmetry planes shown in figure 4.1(a). The axial and non-axial components of the effective field are given by $\Pi_{\parallel} = d_{\parallel}E_z + M_z$ and $\Pi_{x,y} = d_{\perp}E_{x,y} + M_{x,y}$, respectively. Here, $\mathbf{E} = (E_x, E_y, E_z)$ is the electric field vector, and $d_{\parallel} = 0.35 \text{ Hz cmV}^{-1}$ and $d_{\perp} = 17 \text{ Hz cmV}^{-1}$ are the axial and transverse electric field susceptibilities, respectively [6]. The spin-strain

interaction parameters, M_z and $M_{x,y}$, are also included in the effective field vector and depend on the spin-strain susceptibilities. These susceptibilities are of comparable magnitude to the electric field susceptibilities, unlike the case of electric field susceptibilities alone. More details can be found in reference [7]. The dimensionless vector operators for the nuclear and electronic spins are denoted by $\hat{\mathbf{I}} = (\hat{I}_x, \hat{I}_y, \hat{I}_z)$ and $\hat{\mathbf{S}} = (\hat{S}_x, \hat{S}_y, \hat{S}_z)$, respectively. The zero-field splitting parameter is given by $D = 2.87$ GHz, and the axial hyperfine coupling parameter is $A_{HF} = -2.14$ MHz.

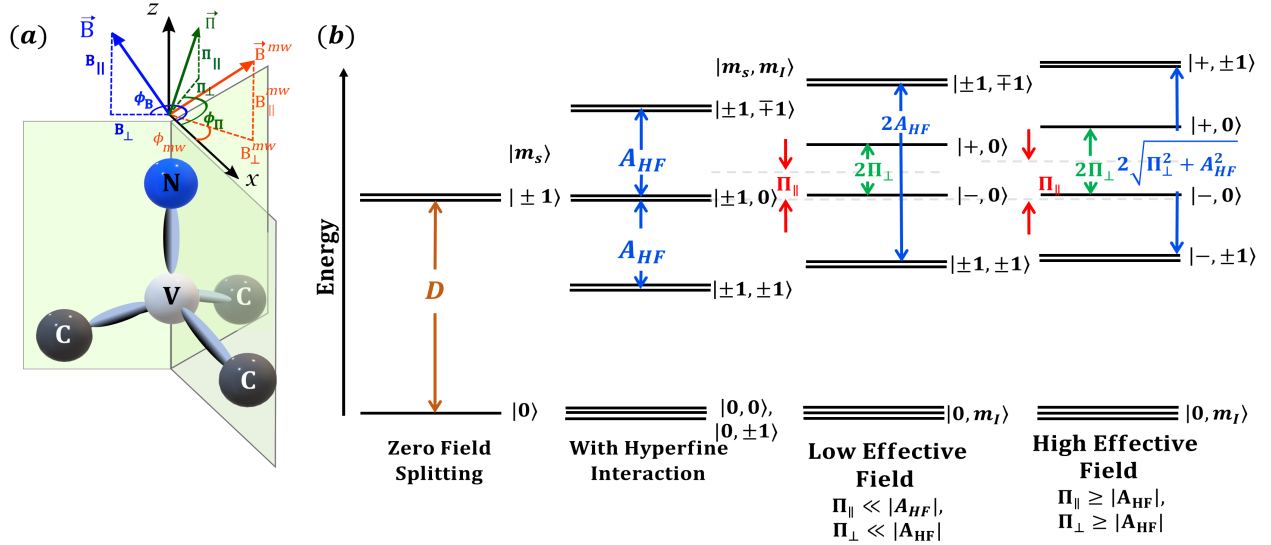


Figure 4.1: (a) The NV axis is parallel to the z-axis in the coordinate system of the NV center. In this system, the microwave (MW) magnetic field used to manipulate the NV spin is shown by a red vector, the external magnetic field is shown by a blue vector, and the intrinsic effective field is denoted by a green vector. (b) The energy levels diagram of the electron-nuclear spin system of the NV center. This diagram highlights the influence of the effective field interaction term in the Hamiltonian, displaying the energy level shifts and splittings in three distinct parameter regimes. These regimes are defined as follows: (i) when Π_\perp and Π_\parallel are both zero, (ii) when $|A_{HF}|$ is much larger than Π_\perp and Π_\parallel , and (iii) when $|A_{HF}| \leq \Pi_\perp$ and Π_\parallel .

4.1.1 Eigenenergies and Eigenstates

The eigenenergies of the hyperfine states in the presence of the intrinsic effective field can be obtained by solving Hamiltonian (4.1.1), which is expressed as

$$E_{|-,0\rangle} = D + \Pi_{\parallel} - \Pi_{\perp}, \quad (4.1.2a)$$

$$E_{|+,0\rangle} = D + \Pi_{\parallel} + \Pi_{\perp}, \quad (4.1.2b)$$

$$E_{|-,+1\rangle} = D + \Pi_{\parallel} - \sqrt{\Pi_{\perp}^2 + |A_{HF}|^2}, \quad (4.1.2c)$$

$$E_{|-,+1\rangle} = D + \Pi_{\parallel} + \sqrt{\Pi_{\perp}^2 + |A_{HF}|^2}, \quad (4.1.2d)$$

$$E_{|-, -1\rangle} = D + \Pi_{\parallel} - \sqrt{\Pi_{\perp}^2 + |A_{HF}|^2}, \quad (4.1.2e)$$

$$E_{|+, -1\rangle} = D + \Pi_{\parallel} + \sqrt{\Pi_{\perp}^2 + |A_{HF}|^2}, \quad (4.1.2f)$$

The transverse effective field amplitudes denoted by $\Pi_{\perp} = \sqrt{\Pi_x^2 + \Pi_y^2}$. The associated hyperfine eigenstates can be written in the uncoupled basis $|m_s, m_I\rangle = |m_s\rangle \otimes |m_I\rangle$ as follows:

$$|-, 0\rangle = \frac{1}{\sqrt{2}} (|+1\rangle - e^{i\phi_{\Pi}} |-1\rangle) \otimes |0\rangle, \quad (4.1.3a)$$

$$|+, 0\rangle = \frac{1}{\sqrt{2}} (|+1\rangle + e^{i\phi_{\Pi}} |-1\rangle) \otimes |0\rangle, \quad (4.1.3b)$$

$$|-, +1\rangle = \left(\sin \frac{\theta_{\Pi}}{2} |+1\rangle - e^{i\phi_{\Pi}} \cos \frac{\theta_{\Pi}}{2} |-1\rangle \right) \otimes |+1\rangle, \quad (4.1.3c)$$

$$|+, +1\rangle = \left(\cos \frac{\theta_{\Pi}}{2} |+1\rangle + e^{i\phi_{\Pi}} \sin \frac{\theta_{\Pi}}{2} |-1\rangle \right) \otimes |+1\rangle, \quad (4.1.3d)$$

$$|-, -1\rangle = \left(\cos \frac{\theta_{\Pi}}{2} |+1\rangle - e^{i\phi_{\Pi}} \sin \frac{\theta_{\Pi}}{2} |-1\rangle \right) \otimes |-1\rangle, \quad (4.1.3e)$$

$$|+, -1\rangle = \left(\sin \frac{\theta_{\Pi}}{2} |+1\rangle + e^{i\phi_{\Pi}} \cos \frac{\theta_{\Pi}}{2} |-1\rangle \right) \otimes |-1\rangle, \quad (4.1.3f)$$

where θ_{Π} and ϕ_{Π} are the angles which satisfy the relations

$$\cos \theta_{\Pi} = \frac{-|A_{HF}|}{\sqrt{\Pi_{\perp}^2 + |A_{HF}|^2}}, \quad (4.1.4a)$$

$$\cos \phi_{\Pi} = \frac{\Pi_x}{\Pi_{\perp}}. \quad (4.1.4b)$$

Additionally, Eigenenergies and Eigen states for a low effective field are described in Appendix A.3, and its energy-level diagram is depicted in figure 4.1(a).

4.2 Experimental results of two different effective field regimes

figure 4.2 shows the high-resolution pulsed ODMR spectrum of a single NV of type Ib HPHT sample as well as a poly-crystalline diamond sample. We studied two different regimes of the effective field through this experimental data, which is discussed below:

4.2.1 Low effective field regime ($\Pi_{\perp} \ll |A_{HF}|$)

The hyperfine coupling between the NV spin and the ^{14}N nucleus is significantly bigger than the transverse component of the effective field in this regime. However, central transitions $|\pm 1, 0\rangle$ are coupled with each other and split by $2\Pi_{\perp}$. Contrarily, the mixing states $| -1, +1 \rangle$ & $| +1, +1 \rangle$ and $| -1, -1 \rangle$ & $| +1, -1 \rangle$ due to the hyperfine coupling parameter A_{HF} limiting the effective field. As a result, the effective field has no influence on the outer transition frequencies; rather, it merely causes the hyperfine projections with the same m_I to be split by $2|A_{HF}|$, as it would in the case of a Hamiltonian without an effective field (see figure 4.1(b)).

Figure 4.2(a) shows the experimental studies of a single NV in this effective field regime. We perform pulsed ODMR measurement on a single NV of type Ib diamond sample. By analysing data, we observed the shift in the overall spectrum is $\Pi_{\parallel} \approx 50 \text{ kHz}$, while the split between central transitions is $2\Pi_{\perp} \approx 500 \text{ kHz}$.

4.2.2 High effective field regime ($\Pi_{\perp} \gtrsim |A_{HF}|$)

When the transverse component of the effective field has a similar or higher magnitude to the hyperfine splitting, the states $| -1, +1 \rangle$ & $| +1, +1 \rangle$ and $| -1, -1 \rangle$ & $| +1, -1 \rangle$ can interact to form two new eigenstates with the splitting of $2\sqrt{\Pi_{\perp}^2 + |A_{HF}|^2}$ as depicted in figure 4.1(b). The pulsed ODMR spectrum of a single NV in the PCD sample is presented in figure 4.2(b)

of our experimental data. The spectrum shows a separation of $\Pi_{\perp} = 4.20$ MHz between the inner states $|+, 0\rangle$ and $|-, 0\rangle$, while the shift in the ODMR spectrum from the zero-field splitting is $\Pi_{\parallel} = 4.32$ MHz. By analyzing the shift in the spectrum and the splitting of the central transition frequencies, we can determine the magnitude of the effective field.

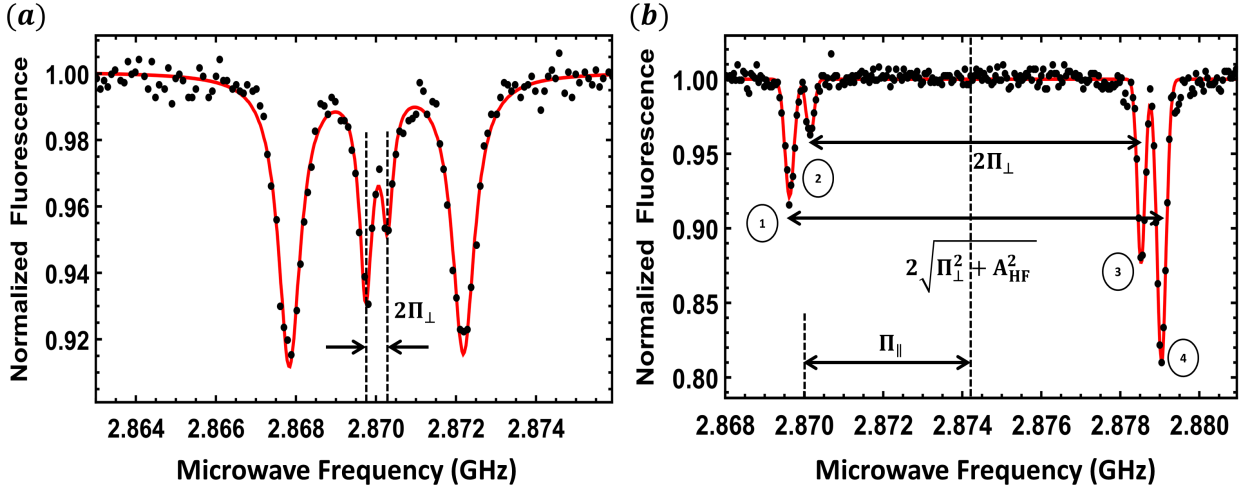


Figure 4.2: The figure shows two high-resolution ODMR spectra of a single NV center in different diamond samples. (a) For the type Ib HPHT diamond sample, we observed the splitting between inner states is $2\Pi_{\perp} \approx 500$ kHz and shift in the overall spectrum is $\Pi_{\parallel} \approx 50$ kHz, which indicate low effective field regime. (b) For the PCD sample, the spectrum shows a large shifting and splitting of both the inner and the outer transitions. The transverse effective field induces a splitting of $2\Pi_{\perp} \approx 8.38$ MHz, while the axial effective field induces a common-mode shift of $\Pi_{\parallel} \approx 4.32$ MHz in the hyperfine energy levels, which indicate the presence of a high effective field in PCD sample.

Our paper [18] presents a novel observation of the mixing of outer state at zero magnetic field in a highly effective field regime, which was not observed previously. A thorough study of the effective field and its impact on the transition strength is also given in our paper.

4.3 Transition Imbalance

This section introduces the concept of transition imbalance and mathematically explores the impact of the effective field on the strength or probability of the transitions between the states. Appendix B provides a detailed calculation for determining the interaction Hamil-

tonian for arbitrary polarization of the MW field. The interaction Hamiltonian can be expressed as:

$$\hat{H}_I^{mw} = \frac{\gamma B_{mw}}{2} \begin{bmatrix} 0 & \cos\left(\frac{\pi}{4} - \epsilon_{mw}\right) e^{-i\phi_{mw}} & 0 \\ \cos\left(\frac{\pi}{4} - \epsilon_{mw}\right) e^{i\phi_{mw}} & 0 & \sin\left(\frac{\pi}{4} - \epsilon_{mw}\right) e^{-i\phi_{mw}} \\ 0 & \sin\left(\frac{\pi}{4} - \epsilon_{mw}\right) e^{i\phi_{mw}} & 0 \end{bmatrix} \quad (4.3.1)$$

The transition strength for transition between $|0, m_I\rangle$ and $|\pm, m_I\rangle$ can be determined by following equation,

$$P_{|\pm, m_I\rangle} \propto |\langle \pm, m_I | H_I^{mw} | 0, m_I \rangle|^2 \quad (4.3.2)$$

the six hyperfine spin transition strengths under driving by an arbitrarily polarized microwave field are given by

$$P_{|-,0\rangle} \propto \left| \frac{1}{\sqrt{2}} \cos\left(\frac{\pi}{4} - \epsilon_{mw}\right) - \frac{1}{\sqrt{2}} \sin\left(\frac{\pi}{4} - \epsilon_{mw}\right) e^{i(2\phi_{mw} - \phi_\Pi)} \right|^2 \quad (4.3.3a)$$

$$P_{|+,0\rangle} \propto \left| \frac{1}{\sqrt{2}} \cos\left(\frac{\pi}{4} - \epsilon_{mw}\right) + \frac{1}{\sqrt{2}} \sin\left(\frac{\pi}{4} - \epsilon_{mw}\right) e^{i(2\phi_{mw} - \phi_\Pi)} \right|^2 \quad (4.3.3b)$$

$$P_{|-,+1\rangle} \propto \left| \sin\left(\frac{\theta_\Pi}{2}\right) \cos\left(\frac{\pi}{4} - \epsilon_{mw}\right) - \cos\left(\frac{\theta_\Pi}{2}\right) \sin\left(\frac{\pi}{4} - \epsilon_{mw}\right) e^{i(2\phi_{mw} - \phi_\Pi)} \right|^2 \quad (4.3.3c)$$

$$P_{|+,+1\rangle} \propto \left| \cos\left(\frac{\theta_\Pi}{2}\right) \cos\left(\frac{\pi}{4} - \epsilon_{mw}\right) + \sin\left(\frac{\theta_\Pi}{2}\right) \sin\left(\frac{\pi}{4} - \epsilon_{mw}\right) e^{i(2\phi_{mw} - \phi_\Pi)} \right|^2 \quad (4.3.3d)$$

$$P_{|-, -1\rangle} \propto \left| \cos\left(\frac{\theta_\Pi}{2}\right) \cos\left(\frac{\pi}{4} - \epsilon_{mw}\right) - \sin\left(\frac{\theta_\Pi}{2}\right) \sin\left(\frac{\pi}{4} - \epsilon_{mw}\right) e^{i(2\phi_{mw} - \phi_\Pi)} \right|^2 \quad (4.3.3e)$$

$$P_{|+, -1\rangle} \propto \left| \sin\left(\frac{\theta_\Pi}{2}\right) \cos\left(\frac{\pi}{4} - \epsilon_{mw}\right) + \cos\left(\frac{\theta_\Pi}{2}\right) \sin\left(\frac{\pi}{4} - \epsilon_{mw}\right) e^{i(2\phi_{mw} - \phi_\Pi)} \right|^2 \quad (4.3.3f)$$

We can calculate transition imbalance from the above transition strength equations. The transition imbalance for inner state with $m_I = 0$ can be defined as [38],

$$\mathcal{I}_{inner} = \frac{P_{|+,0\rangle} - P_{|-,0\rangle}}{P_{|+,0\rangle} + P_{|-,0\rangle}} \quad (4.3.4a)$$

and the transition imbalance of the outer states with $m_I = \pm 1$ transitions is given by

$$\mathcal{I}_{outer} = \frac{P_{|+, \pm 1\rangle} - P_{|-, \pm 1\rangle}}{P_{|+, \pm 1\rangle} + P_{|-, \pm 1\rangle}} \quad (4.3.4b)$$

From equation 4.3.3, we can determine the transition strength of all six states for the linear MW field ($\epsilon_{mw} = 0$). These transition strengths are,

$$P_{|\pm,0\rangle} \propto \frac{1}{2} [1 \pm \cos(2\phi_{mw} - \phi_\Pi)], \quad (4.3.5a)$$

$$P_{|-, \pm 1\rangle} \propto \frac{1}{2} [1 - \sin \theta_\Pi \cos(2\phi_{mw} - \phi_\Pi)], \quad (4.3.5b)$$

$$P_{|+, \pm 1\rangle} \propto \frac{1}{2} [1 + \sin \theta_\Pi \cos(2\phi_{mw} - \phi_\Pi)] \quad (4.3.5c)$$

The transition strength for inner states and outer states can be calculated using equations 4.3.4 and 4.3.5,

$$\mathcal{I}_{inner} = \cos(2\phi_{mw} - \phi_\Pi), \quad (4.3.6a)$$

$$\mathcal{I}_{outer} = \sin \theta_\Pi \cos(2\phi_{mw} - \phi_\Pi) \quad (4.3.6b)$$

Equation 4.3.3 describes how the effective field affects the transition strengths of states. The transition imbalance of the states depends on the MW angle ϕ_{mw} and the azimuthal angle of the effective field ϕ_Π . The equations 4.3.5 and 4.3.4 described the transition strength of all six states and transition imbalance with linear MW polarization. equation 4.3.6 indicates that the degree of imbalance is determined by the relative angle between $2\phi_{mw}$ and ϕ_Π . By analysing experimental data given in figure 4.2(b), The observed values of the imbalance for the outer and inner hyperfine resonances are $\mathcal{I}_{outer} \approx 37.4\%$ and $\mathcal{I}_{inner} \approx 50.8\%$ respectively. While the inner state transition imbalance $\mathcal{I}_{inner} \approx -19.8\%$ is observed for the experimental data given in 4.2(a).

The novel observation of transition imbalance of outer states is reported in our research paper [18]. The study of NV properties with an effective field is essential to make highly sensitive magnetic field sensing devices. These investigations significantly advanced our understanding of the field of quantum technology-based magnetic field sensing.

Chapter 5

Selective Transitions Using Circular MW Field

The ability to control spin transitions in NV centers has significant implications for the development of high-sensitivity magnetometers based on these systems. An attractive approach for treating spin transitions individually is polarization-based microwave (MW) fields [40].

In this chapter, we investigate the selection rule of spin transition using the circularly polarized MW field. We can control the transitions from state $|m_s = 0\rangle$ to $|m_s = +1\rangle$ using σ^+ MW polarization or left-hand circular polarization (LHCP) MW field. Similarly, σ^- MW polarization or right-hand circular polarization (RHCP) MW field facilitates us to control the transition between state $|m_s = 0\rangle$ and $|m_s = -1\rangle$. These spin transitions follow the selection rule and conserve the spin angular momentum during the transition.

We produced σ^+ and σ^- MW polarization using the specially designed PCD as demonstrated by Mrózek et al. in [41]. we were performed CW ODMR with the controlled spin transition using linear, σ^+ and σ^- polarized MW field. The experimental results are shown in figure 5.1. Since The linear polarized MW field can be considered as a superposition of the σ^+ polarization and σ^- polarization, it excites both the transitions from $|m_s = 0\rangle$ to $|m_s = +1\rangle$ and from $|m_s = 0\rangle$ to $|m_s = -1\rangle$ (see figure 5.1(a)). We also observed selective spin transition in figures 5.1(b) and 5.1(c). However, we are not able to get full selectivity. We investigate this problem with a mathematical approach, and a detailed discussion of the

results is given in the next section.

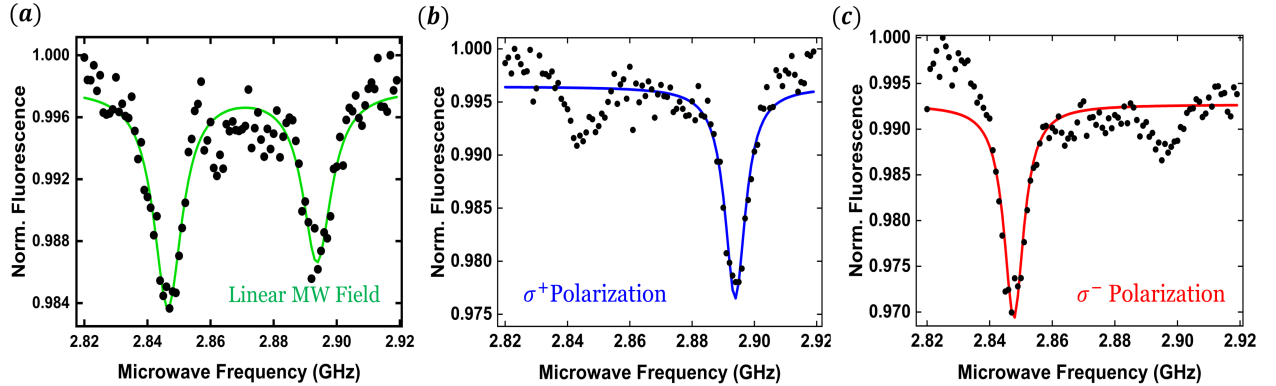


Figure 5.1: Experimental data of CW ODMR using three type of MW field polarization (a) Linear MW polarization (b) σ^+ MW polarization (c) σ^- MW polarization

5.1 Selectivity of spin transitions

In this section, we will mathematically explore the transition strength of the eigenstate of the NV center at a finite magnetic field. Let's consider the NV center make an angle θ_{NV} with the z-axis of the lab frame as depicted in figure 5.2.

We considered $(\hat{x}, \hat{y}, \hat{z})$ as a lab coordinate frame and $(\hat{e}_x, \hat{e}_y, \hat{e}_z)$ as NV coordinate frame. We apply a polarized MW field in the lab frame. Thus we can express σ^+ polarization and σ^- polarization in mathematical form in the lab frame similar to that given in Appendix B,

$$\begin{aligned} \mathbf{B}_{mw,\sigma^+}(t) &= B_{mw} [\cos(\omega t) \hat{x} + \sin(\omega t) \hat{y}] \\ \mathbf{B}_{mw,\sigma^-}(t) &= B_{mw} [\cos(\omega t) \hat{x} - \sin(\omega t) \hat{y}] \end{aligned} \quad (5.1.1)$$

Consider σ^+ polarized MW field is used for drive transition from $|0\rangle$ to $|+1\rangle$. To calculate the transition strength similar to that given in section 4.3, we require interaction Hamiltonian of polarized MW field. The σ^+ polarization equation in 5.1.1 can be

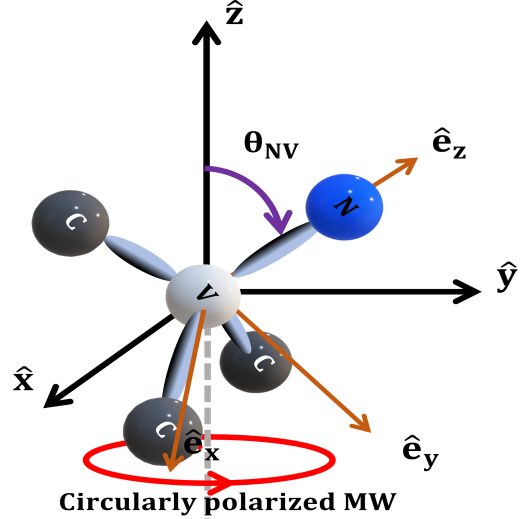


Figure 5.2: NV center diagram: The NV axis make an angle θ_{NV} with the z axis of the lab frame.

expressed in the NV coordinate frame as,

$$\begin{aligned}\mathbf{B}_{mw,\sigma^+}(t) = B_{mw} & \left[\left(\frac{1}{2}(1 + \cos(\theta_{NV})) \cos(\omega t) + \frac{1}{2}(\cos(\theta_{NV}) - 1) \sin(\omega t) \right) \hat{\mathbf{e}}_x \right. \\ & + \left(\frac{1}{2}(\cos(\theta_{NV}) - 1) \cos(\omega t) + \frac{1}{2}(1 + \cos(\theta_{NV})) \sin(\omega t) \right) \hat{\mathbf{e}}_y \\ & \left. - \left(\frac{1}{\sqrt{2}} \sin(\theta_{NV})(\cos(\omega t) + \sin(\omega t)) \right) \hat{\mathbf{e}}_z \right]\end{aligned}$$

However, The $\hat{\mathbf{e}}_z$ component does not affect the spin transition. So we can express the Hamiltonian of σ^+ polarized MW field using equation 2.4.2,

$$\begin{aligned}\hat{H}_{mw,\sigma^+}(t) = (\gamma B_{mw}) & \left[\frac{1}{2}(1 + \cos(\theta_{NV})) \left(\cos(\omega t) \hat{S}_x + \sin(\omega t) \hat{S}_y \right) \right. \\ & \left. + \frac{1}{2}(\cos(\theta_{NV}) - 1) \left(\sin(\omega t) \hat{S}_x + \cos(\omega t) \hat{S}_y \right) \right] \quad (5.1.2)\end{aligned}$$

Hence, the total Hamiltonian of a single NV center at a finite magnetic field is described as,

$$\hat{H}(t) = D \hat{S}_z^2 + \gamma B_z \hat{S}_z + \hat{H}_{mw,\sigma^+}(t) \quad (5.1.3)$$

Equation 5.1.3 can be written in the interaction picture using unitary operator $\hat{U} = e^{i\omega t \hat{S}_z^2}$ and rotating wave approximation (RWA) similar to discussed in Appendix B,

$$\hat{H}_I = D' \hat{S}_z^2 + \gamma B_z \hat{S}_z + \frac{\gamma B_{mw}}{2\sqrt{2}} (1 + \cos(\theta_{NV})) \begin{pmatrix} 0 & 1 & 0 \\ 1 & 0 & 0 \\ 0 & 0 & 0 \end{pmatrix} + \frac{\gamma B_{mw}}{2\sqrt{2}} (\cos(\theta_{NV}) - 1) \begin{pmatrix} 0 & 0 & 0 \\ 0 & 0 & -\iota \\ 0 & \iota & 0 \end{pmatrix} \quad (5.1.4)$$

Finally, we calculate transition strength of transition between $|0\rangle$ to $|+1\rangle$ and $|0\rangle$ to $|+1\rangle$ using equations 4.3.2 and 5.1.4,

$$P_{|0\rangle \rightarrow |+1\rangle} \propto \left| \langle +1 | \hat{H}_I | 0 \rangle \right|^2 = \frac{(\gamma B_{mw})^2}{8} (1 + \cos(\theta_{NV}))^2 \quad (5.1.5a)$$

$$P_{|0\rangle \rightarrow |-1\rangle} \propto \left| \langle -1 | \hat{H}_I | 0 \rangle \right|^2 = \frac{(\gamma B_{mw})^2}{8} (\cos(\theta_{NV}) - 1)^2 \quad (5.1.5b)$$

If we consider a (100) oriented diamond sample, then the NV axis makes an angle $\theta_{NV} \approx 54.7^\circ$ with \hat{z} axis of the lab frame. We can quantitatively calculate transition strength for transition between $|0\rangle$ to $|+1\rangle$ and $|0\rangle$ to $|+1\rangle$ using equations 5.1.6,

$$P_{|0\rangle \rightarrow |+1\rangle} \propto \frac{2 + \sqrt{3}}{12} \quad \text{and} \quad P_{|0\rangle \rightarrow |-1\rangle} \propto \frac{2 - \sqrt{3}}{12} \quad (5.1.6a)$$

These quantitative results are aligned with T.P.M. Alegre et al.'s analysis in [40]. The effect of σ^- polarization on the transition strength can be calculated by following the above calculations. The results of the calculations imply that the orientation of the NV center influences the strength of the state transitions.

5.1.1 Experimental Results

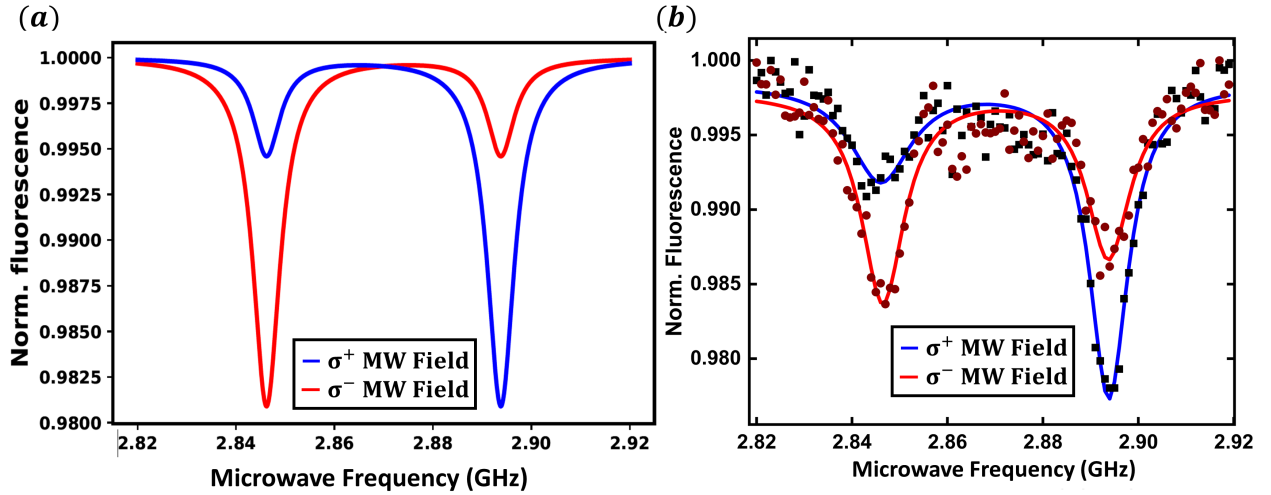


Figure 5.3: (a) The simulation plot depicts the theoretical ODMR spectrum based on transitions strength calculations for both polarization. (b) The experimental ODMR spectrum of a single NV is shown for both polarization.

Based on the equation 5.1.6, we can make a simulation of CW ODMR of a single NV with σ^+ and σ^- polarization as shown in the figure 5.3(a). The experimental data also display in figure 5.3(b). The theoretical transition strength equation 5.1.6 is used for simulation along with Lorentz fit equation. The parameters like linewidth $\Gamma = 3.32$ MHz and $\theta_{NV} = \pi/3$ are being used for simulation. Based on the results shown in figure 5.3, it can be concluded that the experimental observations are consistent with the theoretical calculations.

5.2 Addressing dark state at zero magnetic field using circular MW field

We thoroughly discussed the transition strength of the states and the transition imbalance between states in Chapter 4. We can determine the magnitude of the intrinsic effective field using a pulsed-ODMR high-resolution spectroscopic technique (see section 4.2). The equation 4.3.6(a) represent the imbalance between the inner states $|\pm, 0\rangle$ for linear MW field, which is given as,

$$\mathcal{I}_{inner} = \cos(2\phi_{mw} - \phi_{\Pi}) \quad (5.2.1)$$

According to above equation, we get 100% imbalance for $2\phi_{mw} = \phi_{\Pi}$. In this case, we observed a dark state in the highly-resolved ODMR spectrum as experimental data shown in figure 5.4(a). It is very difficult to determine the magnitude of the intrinsic effective field with this type of ODMR spectra. To tackle this problem, we used circular MW polarization to selectively drive the spin transitions as shown in figures 5.4(b) and 5.4(c). Due to its ability to drive both the bright and dark states, the circular polarization of the MW field allows for the determination of the magnitude of the effective field, even in the presence of a dark state in the ODMR spectrum for a linear MW field at zero magnetic field.

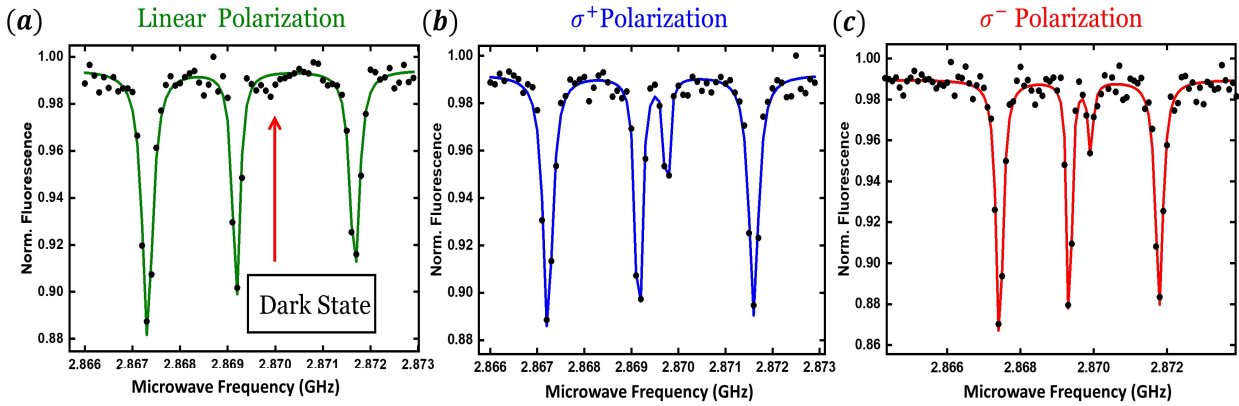


Figure 5.4: (a) Dark state appears in the ODMR spectrum with linear MW field. (b) Both inner states are observed in ODMR spectra with both σ^+ MW polarization and (c) σ^- MW polarization.

We discussed the circular MW polarization and its impact on the transition strength in this chapter. The investigation of the selection rules with both linear and circular MW polarization is proven to be helpful for spin initialization and spin manipulation. Addressing the dark state with circular polarization facilitates us to determine the intrinsic effective field at the zero magnetic field.

Chapter 6

Control of Inner States Transition using Radio Frequency

One of the main aspects of NV-based quantum computations and quantum sensors is the ability to control transitions between the spin states of the NV center [42]. Control of spin transition is essential to exploit the full potential of the Spin-1 NV center. Especially control of spin transition, ease of spin initialization and spin manipulation, which is advanced in the NV center-based quantum sensing technology.

Over the years, various methods such as magnetic fields [43], lasers, mechanical vibrations [44], and electric fields [45] have been investigated to attain full manipulation of three transitions. However, the current approach requires complex fabrication in diamonds to accomplish this level of control at room temperature. This is because the method necessitates either mechanical vibrations [44] or the application of electric fields [45], both of which are challenging to achieve without extensive diamond modification.

In this chapter, We demonstrate the simple method to control the transition between inner states using a Radio frequency (RF) field at zero magnetic fields, based on the techniques given in [42] and [46]. First, we developed a theoretical model for inner state transition at zero magnetic field, and then we compared the result of the theoretical model with experimental data.

6.1 Theoretical model

In this section, we discussed the mathematical model for spin transition between the inner states ($|+, 0\rangle$ and $|-, 0\rangle$) of the NV center at zero magnetic field. The mathematical model explains the experimental method for controlling spin transition between hyperfine states or inner states $|+, 0\rangle$ and $|-, 0\rangle$. The Hamiltonian of the NV center in the presence of an effective field and hyperfine field at zero magnetic field can be given as,

$$\hat{H}_0 = (D + \Pi_{\parallel})\hat{S}_z^2 + A_{HF}\hat{S}_z\hat{I}_z + \Pi_x(\hat{S}_x^2 - \hat{S}_y^2) + \Pi_y(\hat{S}_x\hat{S}_y + \hat{S}_y\hat{S}_x) \quad (6.1.1)$$

Where all symbols represent the same information as given in Chapter 4. In this chapter, we focused only on hyperfine states with $m_I = 0$. Hence, Hamiltonian can be rewritten as,

$$\hat{H}_0 = (D + \Pi_{\parallel})\hat{S}_z^2 + \Pi_x(\hat{S}_x^2 - \hat{S}_y^2) + \Pi_y(\hat{S}_x\hat{S}_y + \hat{S}_y\hat{S}_x) \quad (6.1.2)$$

Eigenenergy of Hamiltonian 6.1.2 can be given by,

$$E_+ = D + \Pi_{\parallel} + \Pi_{\perp} \quad (6.1.3a)$$

$$E_- = D + \Pi_{\parallel} - \Pi_{\perp} \quad (6.1.3b)$$

Eigenstates of Hamiltonian 6.1.2 can be given by,

$$|+, 0\rangle = |B\rangle = \frac{1}{\sqrt{2}}(|+1\rangle + e^{i\phi_{\Pi}}|-1\rangle) \quad (6.1.4a)$$

$$|-, 0\rangle = |D\rangle = \frac{1}{\sqrt{2}}(|+1\rangle - e^{i\phi_{\Pi}}|-1\rangle) \quad (6.1.4b)$$

Where, $\Pi_{\perp} = \sqrt{\Pi_x^2 + \Pi_y^2}$ and $\phi_{\Pi} = \tan^{-1}\left(\frac{\Pi_y}{\Pi_x}\right)$. We considered $|0, 0\rangle$ as $|0\rangle$, $|+, 0\rangle$ as bright state $|B\rangle$ and $|-, 0\rangle$ as dark state $|D\rangle$ throughout this chapter. For further calculation, We redefined Hamiltonian 6.1.2 such that Π_x and Π_y in the form of Π_{\perp} ,

$$\hat{H}_0 = (D + \Pi_{\parallel})\hat{S}_z^2 + \Pi_{\perp}(|B\rangle\langle B| - |D\rangle\langle D|) \quad (6.1.5)$$

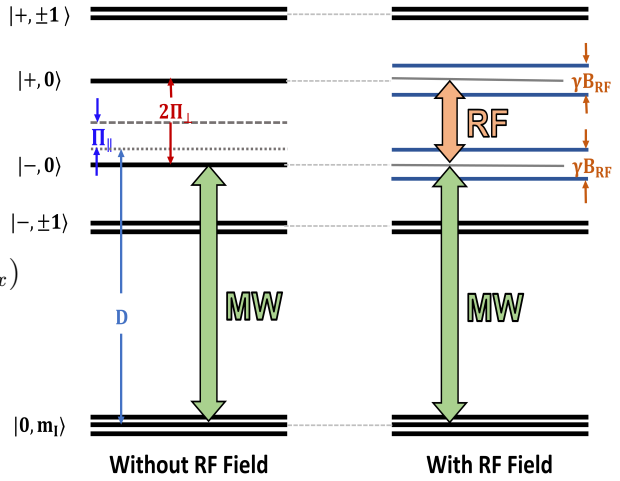


Figure 6.1: Energy-level diagram of NV center at zero magnetic field with and without RF

As we discussed earlier in Chapter 4, The MW field is utilized to drive spin transition from $|0\rangle$ to $|B\rangle$ and from $|0\rangle$ to $|D\rangle$. While the transition between $|B\rangle$ and $|D\rangle$ is controlled by the RF field. Hence, the Hamiltonian containing MW field and RF field can be described by,

$$\hat{H}_{mw}(t) = \Omega_{mw}^x \hat{S}_x \cos(\omega_{mw}t) + \Omega_{mw}^y \hat{S}_y \cos(\omega_{mw}t) \text{ and } \hat{H}_{RF}(t) = \Omega_{RF}^z \hat{S}_z \cos(\omega_{RF}t) \quad (6.1.6)$$

$\Omega_{mw}^{x,y} = \gamma B^{x,y}$ and $\Omega_{RF}^z = \gamma B^z$ represent the strength of the MW field and RF field, respectively. From equations 6.1.5 and 6.1.6, the total Hamiltonian is given by,

$$\hat{H}(t) = (D + \Pi_{\parallel}) \hat{S}_z^2 + \Pi_{\perp}(|B\rangle \langle B| - |D\rangle \langle D|) + \hat{H}_{mw}(t) + \hat{H}_{RF}(t) \quad (6.1.7)$$

Now, We use equation B.1.4 and RWA to determine the rotating frame Hamiltonian with different unitary operators in the following three steps:

- **Step:1**

The unitary operator $\hat{U}_1 = \exp\left\{-i \omega_{mw} t \hat{S}_z^2\right\}$ act on the equation 6.1.7 and give following equation,

$$\begin{aligned} \hat{H}_{I1}(t) &= (D + \Pi_{\parallel} - \omega_{mw}) \hat{S}_z^2 + \Pi_{\perp}(|B\rangle \langle B| - |D\rangle \langle D|) \\ &\quad + \frac{\Omega_{mw}^x}{2} \hat{S}_x + \frac{\Omega_{mw}^y}{2} \hat{S}_y + \Omega_{RF}^z \hat{S}_z \cos(\omega_{RF}t) \end{aligned} \quad (6.1.8)$$

- **Step:2**

We use another unitary operator $\hat{U}_2 = \exp\left\{\frac{i}{2} \omega_{RF} t (|B\rangle \langle B| - |D\rangle \langle D|)\right\}$ on the equation 6.1.8,

$$\begin{aligned} \hat{H}_{I2}(t) &= (D + \Pi_{\parallel} - \omega_{mw} + \Pi_{\perp} - \frac{\omega_{RF}}{2}) |B\rangle \langle B| + (D + \Pi_{\parallel} - \omega_{mw} - \Pi_{\perp} + \frac{\omega_{RF}}{2}) |D\rangle \langle D| \\ &\quad + \frac{\Omega_{RF}^z}{2} \hat{S}_z + \cos\left(\frac{\omega_{RF}t}{2}\right) \left(\frac{\Omega_{mw}^x}{2} \hat{S}_x + \frac{\Omega_{mw}^y}{2} \hat{S}_y \right) \\ &\quad + i \sin\left(\frac{\omega_{RF}t}{2}\right) \left(e^{-i\phi_{\Pi}} \left(\frac{\Omega_{mw}^x}{2\sqrt{2}} + i \frac{\Omega_{mw}^y}{2\sqrt{2}} \right) |+1\rangle \langle 0| - h.c. \right) \\ &\quad + i \sin\left(\frac{\omega_{RF}t}{2}\right) \left(e^{i\phi_{\Pi}} \left(\frac{\Omega_{mw}^x}{2\sqrt{2}} - i \frac{\Omega_{mw}^y}{2\sqrt{2}} \right) |-1\rangle \langle 0| - h.c. \right) \end{aligned} \quad (6.1.9)$$

here, h.c. represents hermitian conjugate.

- Step:3

Equation 6.1.9 contain time-independent and time-dependent terms, which can be expressed as,

$$\hat{H}_{ind} = (D + \Pi_{\parallel} - \omega_{mw})\hat{S}_z^2 + (\Pi_{\perp} - \frac{\omega_{RF}}{2})(|B\rangle\langle B| - |D\rangle\langle D|) + \frac{\Omega_z^{RF}}{2}\hat{S}_z \quad (6.1.10a)$$

$$\begin{aligned} \hat{H}_{dep}(t) &= \cos\left(\frac{\omega_{RF}t}{2}\right)\left(\frac{\Omega_{mw}^x}{2}\hat{S}_x + \frac{\Omega_{mw}^y}{2}\hat{S}_y\right) \\ &\quad + i\sin\left(\frac{\omega_{RF}t}{2}\right)\left(e^{-i\phi_{\Pi}}\left(\frac{\Omega_{mw}^x}{2\sqrt{2}} + i\frac{\Omega_{mw}^y}{2\sqrt{2}}\right)|+1\rangle\langle 0| - h.c.\right) \\ &\quad + i\sin\left(\frac{\omega_{RF}t}{2}\right)\left(e^{i\phi_{\Pi}}\left(\frac{\Omega_{mw}^x}{2\sqrt{2}} - i\frac{\Omega_{mw}^y}{2\sqrt{2}}\right)|-1\rangle\langle 0| - h.c.\right) \end{aligned} \quad (6.1.10b)$$

Since the RF field acts as AC magnetic field, It has a time-varying term in the rotating frame. We now invoke time-dependent perturbation theory to determine the resonance frequency of the MW field with a simultaneously applied RF field. Here equation 6.1.10(b) is considered a time-dependent perturbation. We set RF frequency as $\omega_{RF} = 2\Pi_{\perp}$ during the experiment. Hence, the time-independent Hamiltonian can be written as,

$$\hat{H}'_{ind} = (D + \Pi_{\parallel} - \omega_{mw})\hat{S}_z^2 + \frac{\Omega_z^{RF}}{2}\hat{S}_z \quad (6.1.11)$$

We use a unitary operator $\hat{U} = \exp\{-i\hat{H}'_{ind}t\}$ to utilize time-dependent perturbation theory,

$$\begin{aligned} \hat{H}_I &= \hat{U}^\dagger \hat{H}_{dep}(t) \hat{U} \\ &= \frac{\Omega_{mw}^x}{8} \left[\left((e^{iPt} + e^{iQt}) - e^{-i\phi_{\Pi}}(e^{iPt} - e^{iQt}) \right) (|B\rangle\langle 0| + |D\rangle\langle 0|) \right. \\ &\quad \left. + \left((e^{iRt} + e^{iSt})e^{-i\phi_{\Pi}} - (e^{iRt} - e^{iSt}) \right) (|B\rangle\langle 0| - |D\rangle\langle 0|) + h.c. \right] \\ &\quad + \frac{\Omega_{mw}^y}{8} \left[-i \left((e^{iPt} + e^{iQt}) + e^{-i\phi_{\Pi}}(e^{iPt} - e^{iQt}) \right) (|B\rangle\langle 0| + |D\rangle\langle 0|) \right. \\ &\quad \left. + i \left((e^{iRt} + e^{iSt})e^{-i\phi_{\Pi}} - (e^{iRt} - e^{iSt}) \right) (|B\rangle\langle 0| - |D\rangle\langle 0|) + h.c. \right] \end{aligned}$$

where P, Q, R, S are constants and are given as,

$$P = (D + \Pi_{\parallel} + \frac{\Omega_z^{RF}}{2} - \frac{\omega_{RF}}{2} - \omega_{mw}) \quad (6.1.12a)$$

$$Q = (D + \Pi_{\parallel} + \frac{\Omega_z^{RF}}{2} + \frac{\omega_{RF}}{2} - \omega_{mw}) \quad (6.1.12b)$$

$$R = (D + \Pi_{\parallel} - \frac{\Omega_z^{RF}}{2} - \frac{\omega_{RF}}{2} - \omega_{mw}) \quad (6.1.12c)$$

$$S = (D + \Pi_{\parallel} - \frac{\Omega_z^{RF}}{2} + \frac{\omega_{RF}}{2} - \omega_{mw}) \quad (6.1.12d)$$

Thus, the MW resonance frequency can be determined from equation 6.1.12, while the RF field with frequency $\omega_{RF} = 2\Pi_{\perp}$ is applied simultaneously,

$$\omega_{mw,P} = (D + \Pi_{\parallel} + \Pi_{\perp} - \frac{\omega_{RF}}{2}) \quad (6.1.13a)$$

$$\omega_{mw,Q} = (D + \Pi_{\parallel} + \Pi_{\perp} + \frac{\omega_{RF}}{2}) \quad (6.1.13b)$$

$$\omega_{mw,R} = (D + \Pi_{\parallel} - \Pi_{\perp} - \frac{\omega_{RF}}{2}) \quad (6.1.13c)$$

$$\omega_{mw,S} = (D + \Pi_{\parallel} - \Pi_{\perp} + \frac{\omega_{RF}}{2}) \quad (6.1.13d)$$

To compare the result of this theoretical model with experimental data, we simulate the CW ODMR plot based on equations 6.1.13. Additionally, we depicted the energy level diagram with and without RF field based on equation 6.1.13 in figure 6.1.

6.2 Experimental result

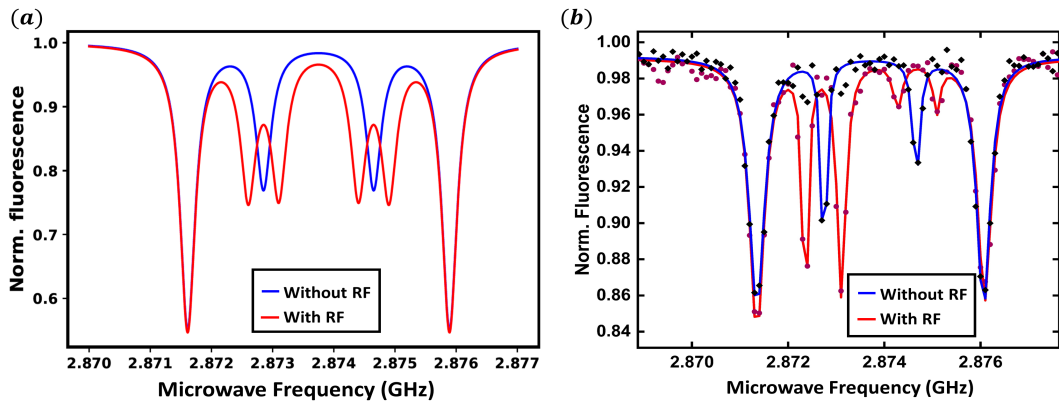


Figure 6.2: (a) The simulation plot of the hyperfine spectrum at zero magnetic field with and without RF field. (b) High-resolution hyperfine spectrum of a single NV center at zero magnetic field with and without RF field.

Based on equation 6.1.13, The simulation plot of the hyperfine spectrum of a single NV center at zero magnetic field is shown in figure 6.2(a). The Lorentz fitting equation with the following parameters is used to produce this simulation: Linewidth (Γ) = 0.15 MHz, Hyperfine parameter (A_{HF}) = -2.14 MHz, and Effective field components: $\Pi_{\parallel} = 3.75$ MHz, and $\Pi_{\perp} = 0.9$ MHz. As discussed in section 6.1, we performed pulsed ODMR measurement on a single NV at zero magnetic field. As the model suggests, first, we got a highly resolved ODMR spectrum of a single NV at zero magnetic field. Then, We determined the value of $2\Pi_{\perp}$ from the splitting of inner states $|B\rangle$ and $|D\rangle$, which is 2.14 MHz, as can seen in figure 6.2(b). Finally, we simultaneously applied the RF field with frequency $\omega_{RF} = 2\Pi_{\perp} = 2.14$ MHz along with the MW field. Imbalance observed in figure 6.2(b) is due to relative angle between $2\phi_{mw}$ and ϕ_{Π} (see section 4.3). The splitting of the inner state depends on the strength of the RF field (γB_{RF}). Hence, It is also used for determining the magnitude of the AC magnetic field.

We described the novel calculations for inner state transition in this chapter. The experimental results perfectly align with the results of the theoretical model, as we can see in figure 6.2. This technique is also useful for determining the magnitude of the AC magnetic field from the splitting of the inner states. The approach presented in this chapter provides a pathway to unlock the complete potential of a spin-1 system.

Chapter 7

MW Polarization-Assisted Vector Magnetometry Using Ensemble of NV Centers

The ability to measure both the strength and direction of magnetic fields are essential in numerous scientific disciplines, including material science, geophysics, and biomedical imaging. In recent years, the nitrogen-vacancy center (NV) in a diamond has emerged as a sensitive magnetic field sensor, and researchers have been exploring its potential applications in these fields. Particularly, there has been promising research on utilizing an ensemble of NV centers to reconstruct the complete vector magnetic field. Various techniques have been employed, including a combination of laser polarization and ODMR measurements [47], as well as the maximum-likelihood method with obtained ODMR data [48]. This chapter presents a new and innovative method for full vector magnetometry that involves rotating the MW polarization.

In our magnetometry approach, we utilize an ensemble of nitrogen-vacancy (NV) centers in a diamond crystal to investigate magnetic fields. Specifically, we observe the transition strengths as a function of the MW polarization angle. An ensemble of NV centers is a high-density collection of multiple NV centers with different orientations in a diamond crystal. Such an ensemble can be utilized for various applications such as quantum entanglement studies [49], magnetic field sensing [50], and biological sample imaging [51]. The ensemble of

NV centers being used in our magnetometry approach comprises four NV centers oriented in different directions, as depicted in figure 7.1. We utilize the (100) oriented diamond sample for our experiments. As shown in figure 7.1, all four families of NV centers in the ensemble are located along the diagonal of the diamond lattice for the (100) orientation. These four families of NV centers are defined as $[1\ 1\ 1]$, $[\bar{1}\ 1\ \bar{1}]$, $[\bar{1}\ \bar{1}\ 1]$ and $[1\ \bar{1}\ \bar{1}]$.

To reconstruct the magnetic field, we utilize the projection of the applied magnetic field vector on each NV axis. The ODMR spectrum for the ensemble exhibits a total of eight resonance peaks at a finite magnetic field, with each orientation of the NV centers contributing two resonance peaks to the spectrum (see figure 7.3). However, identifying which pair of resonance peaks correspond to all four NV orientations has been a significant challenge in vector magnetometry. To address this issue, we present a novel technique for vector magnetometry that utilizes MW polarization. This chapter provides a detailed description of the theoretical model underlying our technique and presents simulation results based on the model. Additionally, we outline the procedure for constructing a magnetic field vector using our approach.

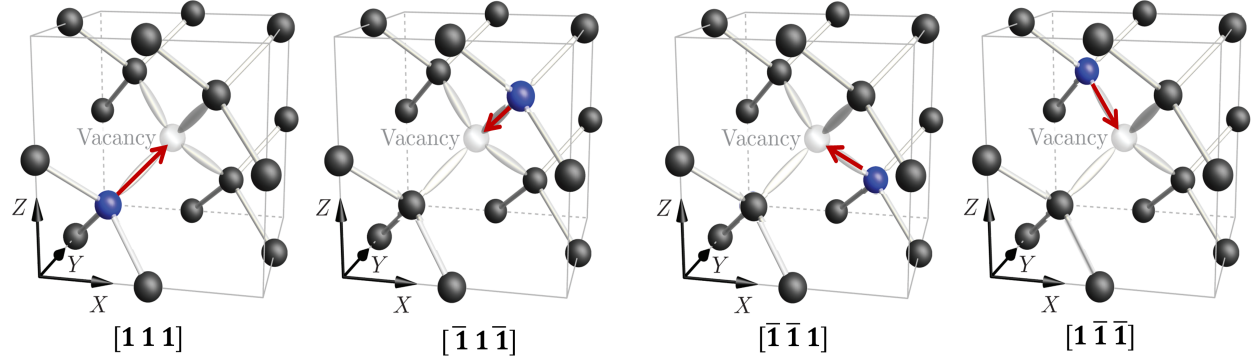


Figure 7.1: All four orientations of NV centers for (100)-oriented diamond sample. The red arrow represents the direction of the NV orientation. These directions are quantitatively written at the bottom of each lattice cell

7.1 Study of spin transition strength as a function of MW polarization angle

In this section, we thoroughly examine the relationship between the MW polarization angle and the strength of the spin transition. As illustrated in figure 7.1, we consider a diamond unit cell coordinate system as (X, Y, Z). External magnetic field vector is defined as $\mathbf{B} = (B_X, B_Y, B_Z)$ in the lab frame. Similarly, the MW field for driving spin transitions is defined as $\mathbf{B}_{mw}(t) = B_{mw}(\sin \theta_{mw} \cos \phi_{mw}, \sin \theta_{mw} \sin \phi_{mw}, \cos \theta_{mw}) \cos(\omega t)$ in the lab frame. Where MW field vector makes θ_{mw} angle with Z-axis and its perpendicular component parameterized by azimuthal angle ϕ_{mw} .

7.1.1 Four orientations of NV centers

In the context of (100) oriented diamond samples, figure 7.1 displays the four possible orientations of NV centers. To better comprehend the theoretical model, we introduce some terminology. We designate each of the NV orientation families as $NV_{i=1,2,3,4}$, which corresponds to the orientations [1 1 1], [1̄ 1 1̄], [1̄ 1̄ 1] and [1 1̄ 1̄], respectively. The NV centers in the samples have two electric dipoles perpendicular to the NV axis. The dipoles' orientation can be determined because they are both perpendicular to the NV orientation axis and each other. We consider the NV orientation axis as $\hat{\mathbf{e}}_z$ and the two dipole orientations as $\hat{\mathbf{e}}_x$ and $\hat{\mathbf{e}}_y$. The NV coordinates for each family can be expressed as follows:

i	NV_i	$\hat{\mathbf{e}}_x$	$\hat{\mathbf{e}}_y$	$\hat{\mathbf{e}}_z$
1	[1 1 1]	(1, 1̄, 0)	(1, 1, 2̄)	(1, 1, 1)
2	[1̄ 1 1̄]	(1, 1, 0)	(1, 1̄, 2̄)	(1̄, 1, 1̄)
3	[1̄ 1̄ 1]	(1̄, 1, 0)	(1̄, 1̄, 2̄)	(1̄, 1̄, 1)
4	[1 1̄ 1̄]	(1̄, 1̄, 0)	(1̄, 1, 2̄)	(1, 1̄, 1̄)

We discuss the calculation of transition strength for each orientation family using the above NV coordinate system.

7.1.2 MW angle dependent transition strength for each orientation family

In order to investigate the transition strength of states, we must determine the Hamiltonian for each orientation family. We transform the external magnetic field vector and the MW field vector from the lab frame to the NV orientation coordinates for each orientation family to construct the Hamiltonian. As discussed earlier, the external magnetic field vector in the lab frame is defined as $\mathbf{B} = (B_X, B_Y, B_Z)$ and a driving MW field can be expressed in a lab frame as,

$$\mathbf{B}_{mw}(t) = B_{mw} \cos(\omega t) \left(\sin \theta_{mw} \cos \phi_{mw}, \sin \theta_{mw} \sin \phi_{mw}, \cos \theta_{mw} \right) \quad (7.1.1)$$

Let's discuss the calculation of transition strength or transition probability for the NV orientation axis [1 1 1], referred to as NV_1 family.

To calculate the transition probability, we need to determine the magnetic field experienced by the [1 1 1] oriented NV center family in the ensemble. This can be done by taking the projection of the lab frame external magnetic field vector on the NV orientation axis, which can be expressed as:

$$B_1 = \frac{1}{\sqrt{3}}(B_X + B_Y + B_Z) \quad (7.1.2)$$

However, we neglect the magnetic field components along the $\hat{\mathbf{e}}_x$ and $\hat{\mathbf{e}}_y$ directions due to their negligible effect on the ODMR spectrum compared to the Zeeman splitting.

We also need to transform the lab frame MW field vector into the NV coordinate system. Since the MW field component along the NV orientation axis ($\hat{\mathbf{e}}_z$) has no impact on the spin transition, we focus only on the MW field component along the $\hat{\mathbf{e}}_x$ and $\hat{\mathbf{e}}_y$ directions. This can be expressed as:

$$\mathbf{B}_{mw1}^x = B_{mw} \cos(\omega t) \left[\sin(\theta_{mw}) \cos\left(\phi_{mw} + \frac{\pi}{4}\right) \right] \hat{\mathbf{e}}_x \quad (7.1.3a)$$

$$\mathbf{B}_{mw1}^y = \frac{1}{\sqrt{3}} B_{mw} \cos(\omega t) \left[-\sqrt{2} \cos(\theta_{mw}) + \sin(\theta_{mw}) \sin\left(\phi_{mw} + \frac{\pi}{4}\right) \right] \hat{\mathbf{e}}_y \quad (7.1.3b)$$

So Hamiltonian for a single NV center at a finite magnetic field with spin transition driving

MW field can be described as,

$$\begin{aligned}\hat{H}_1(t) &= D\hat{S}_z^2 + \gamma B_1 \hat{S}_z + \gamma \mathbf{B}_{mw}(\mathbf{t}) \cdot \hat{\mathbf{S}} \\ &= D\hat{S}_z^2 + \frac{\gamma}{\sqrt{3}}(B_X + B_Y + B_Z)\hat{S}_z + \Omega_{mw} \cos(\omega t) \sin(\theta_{mw}) \cos\left(\phi_{mw} + \frac{\pi}{4}\right)\hat{S}_x \quad (7.1.4) \\ &\quad + \frac{\Omega_{mw}}{\sqrt{3}} \cos(\omega t) \left(-\sqrt{2} \cos(\theta_{mw}) + \sin(\theta_{mw}) \sin\left(\phi_{mw} + \frac{\pi}{4}\right) \right) \hat{S}_y\end{aligned}$$

Where $\Omega_{mw} = \gamma B_{mw}$ represents the strength of the MW field. We can write equation 7.1.4 in the interaction picture using unitary operator $\hat{U} = e^{i\omega t \hat{S}_z^2}$ and rotating wave approximation (RWA) as thoroughly discussed in appendix B.1,

$$\begin{aligned}\hat{H}_{I1} &= D'\hat{S}_z^2 + \frac{\gamma}{\sqrt{3}}(B_X + B_Y + B_Z)\hat{S}_z + \frac{\Omega_{mw}}{2} \sin(\theta_{mw}) \cos\left(\phi_{mw} + \frac{\pi}{4}\right)\hat{S}_x \quad (7.1.5) \\ &\quad + \frac{\Omega_{mw}}{2\sqrt{3}} \left(-\sqrt{2} \cos(\theta_{mw}) + \sin(\theta_{mw}) \sin\left(\phi_{mw} + \frac{\pi}{4}\right) \right) \hat{S}_y\end{aligned}$$

Finally, we can calculate the transition probability/strength or contrast using the equation 2.4.3,

$$C_1 = P_{|0\rangle \rightarrow |\pm 1\rangle} \approx \frac{\Omega_{mw}^2}{8} \left[\sin^2(\theta_{mw}) \cos^2\left(\phi_{mw} + \frac{\pi}{4}\right) + \frac{1}{3} \left(-\sqrt{2} \cos(\theta_{mw}) + \sin(\theta_{mw}) \sin\left(\phi_{mw} + \frac{\pi}{4}\right) \right)^2 \right] \quad (7.1.6)$$

Hence, the above equation 7.1.6 suggest the transition strength or contrast dependent on the orientation of the MW field.

To calculate the transition strength for the $[\bar{1}\bar{1}\bar{1}]$, $[1\bar{1}\bar{1}]$ and $[\bar{1}\bar{1}1]$ oriented NV centers, we follow a similar method as described for the $[111]$ oriented NV center. The time-dependent Hamiltonian, rotating frame Hamiltonian and transition strength for remaining oriented NV center families are given below:

- **$[\bar{1}1\bar{1}]$ -oriented NV center family (NV_2):**

The time-dependent Hamiltonian can be expressed as

$$\begin{aligned}\hat{H}_2 &= D\hat{S}_z^2 + \frac{\gamma}{\sqrt{3}}(-B_X + B_Y - B_Z)\hat{S}_z + \Omega_{mw} \cos(\omega t) \sin(\theta_{mw}) \sin\left(\phi_{mw} + \frac{\pi}{4}\right)\hat{S}_x \\ &\quad + \frac{\Omega_{mw}}{\sqrt{3}} \cos(\omega t) \left(-\sqrt{2} \cos(\theta_{mw}) + \sin(\theta_{mw}) \cos\left(\phi_{mw} + \frac{\pi}{4}\right) \right) \hat{S}_y \quad (7.1.7)\end{aligned}$$

Hamiltonian in the interaction picture can be written as,

$$\begin{aligned}\hat{H}_{I2} = & D' \hat{S}_z^2 + \frac{\gamma}{\sqrt{3}} (-B_X + B_Y - B_Z) \hat{S}_z + \frac{\Omega_{mw}}{2} \sin(\theta_{mw}) \sin\left(\phi_{mw} + \frac{\pi}{4}\right) \hat{S}_x \\ & + \frac{\Omega_{mw}}{2\sqrt{3}} \left(-\sqrt{2} \cos(\theta_{mw}) + \sin(\theta_{mw}) \cos\left(\phi_{mw} + \frac{\pi}{4}\right) \right) \hat{S}_y\end{aligned}\quad (7.1.8)$$

Transition strength:

$$\begin{aligned}C_2 = P_{|0\rangle \rightarrow |\pm 1\rangle} \approx & \frac{\Omega_{mw}^2}{8} \left[\sin^2(\theta_{mw}) \sin^2\left(\phi_{mw} + \frac{\pi}{4}\right) \right. \\ & \left. + \frac{1}{3} \left(-\sqrt{2} \cos(\theta_{mw}) + \sin(\theta_{mw}) \cos\left(\phi_{mw} + \frac{\pi}{4}\right) \right)^2 \right]\end{aligned}\quad (7.1.9)$$

- **[1̄ 1̄ 1]-oriented NV center family (NV_3):**

The time-dependent Hamiltonian can be expressed as

$$\begin{aligned}\hat{H}_3 = & D \hat{S}_z^2 + \frac{\gamma}{\sqrt{3}} (-B_X - B_Y + B_Z) \hat{S}_z - \Omega_{mw} \cos(\omega t) \sin(\theta_{mw}) \cos\left(\phi_{mw} + \frac{\pi}{4}\right) \hat{S}_x \\ & + \frac{\Omega_{mw}}{\sqrt{3}} \cos(\omega t) \left(-\sqrt{2} \cos(\theta_{mw}) - \sin(\theta_{mw}) \sin\left(\phi_{mw} + \frac{\pi}{4}\right) \right) \hat{S}_y\end{aligned}\quad (7.1.10)$$

Hamiltonian in the interaction picture can be written as,

$$\begin{aligned}\hat{H}_{I3} = & D' \hat{S}_z^2 + \frac{\gamma}{\sqrt{3}} (-B_X - B_Y + B_Z) \hat{S}_z - \frac{\Omega_{mw}}{2} \sin(\theta_{mw}) \cos\left(\phi_{mw} + \frac{\pi}{4}\right) \hat{S}_x \\ & + \frac{\Omega_{mw}}{2\sqrt{3}} \left(-\sqrt{2} \cos(\theta_{mw}) - \sin(\theta_{mw}) \sin\left(\phi_{mw} + \frac{\pi}{4}\right) \right) \hat{S}_y\end{aligned}\quad (7.1.11)$$

Transition strength:

$$\begin{aligned}C_3 = P_{|0\rangle \rightarrow |\pm 1\rangle} \approx & \frac{\Omega_{mw}^2}{8} \left[\sin^2(\theta_{mw}) \cos^2\left(\phi_{mw} + \frac{\pi}{4}\right) \right. \\ & \left. + \frac{1}{3} \left(-\sqrt{2} \cos(\theta_{mw}) - \sin(\theta_{mw}) \sin\left(\phi_{mw} + \frac{\pi}{4}\right) \right)^2 \right]\end{aligned}\quad (7.1.12)$$

- **[1 1̄ 1]-oriented NV center family (NV_4):**

The time-dependent Hamiltonian can be expressed as

$$\begin{aligned}\hat{H}_4 = & D \hat{S}_z^2 + \frac{\gamma}{\sqrt{3}} (B_X - B_Y - B_Z) \hat{S}_z - \Omega_{mw} \cos(\omega t) \sin(\theta_{mw}) \sin\left(\phi_{mw} + \frac{\pi}{4}\right) \hat{S}_x \\ & + \frac{\Omega_{mw}}{\sqrt{3}} \cos(\omega t) \left(-\sqrt{2} \cos(\theta_{mw}) - \sin(\theta_{mw}) \cos\left(\phi_{mw} + \frac{\pi}{4}\right) \right) \hat{S}_y\end{aligned}\quad (7.1.13)$$

Hamiltonian in the interaction picture can be written as,

$$\begin{aligned}\hat{H}_{I4} = & D' \hat{S}_z^2 + \frac{\gamma}{\sqrt{3}} (B_X - B_Y - B_Z) \hat{S}_z - \frac{\Omega_{mw}}{2} \sin(\theta_{mw}) \sin\left(\phi_{mw} + \frac{\pi}{4}\right) \hat{S}_x \\ & + \frac{\Omega_{mw}}{2\sqrt{3}} \left(-\sqrt{2} \cos(\theta_{mw}) - \sin(\theta_{mw}) \cos\left(\phi_{mw} + \frac{\pi}{4}\right) \right) \hat{S}_y\end{aligned}\quad (7.1.14)$$

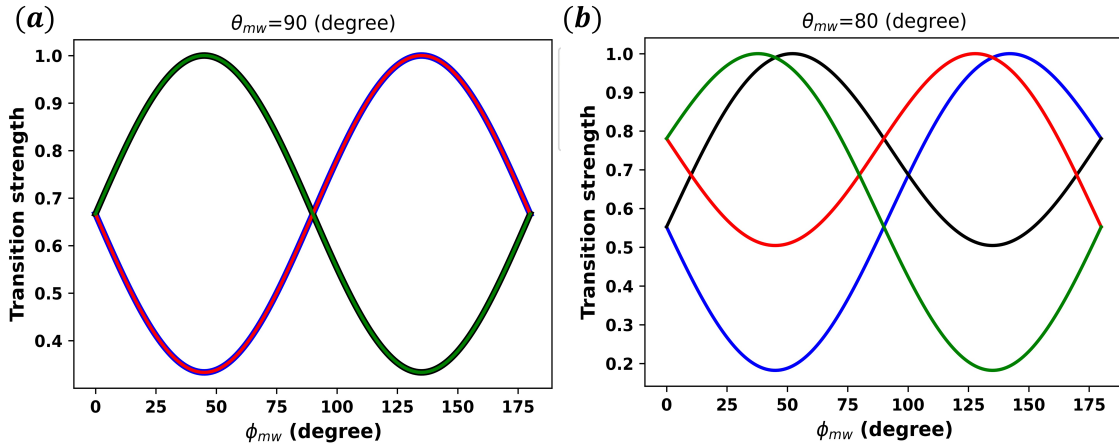
Transition strength:

$$\begin{aligned}C_4 = P_{|0\rangle \rightarrow |\pm 1\rangle} \approx & \frac{\Omega_{mw}^2}{8} \left[\sin^2(\theta_{mw}) \sin^2\left(\phi_{mw} + \frac{\pi}{4}\right) \right. \\ & \left. + \frac{1}{3} \left(-\sqrt{2} \cos(\theta_{mw}) - \sin(\theta_{mw}) \cos\left(\phi_{mw} + \frac{\pi}{4}\right) \right)^2 \right]\end{aligned}\quad (7.1.15)$$

Transition strength for each NV orientation family is dependent on the orientation of the MW field. By utilizing the transition strength equations for each NV orientation, we can simulate the transition strength as a function of MW angles (θ_{mw}, ϕ_{mw}) . This theoretical model provided in this section is crucial for comprehensively grasping our novel technique for vector magnetometry.

7.1.3 Simulation Results

Based on transition strength equations 7.1.5, 7.1.8, 7.1.11 and 7.1.14, we produce the transition strength simulation plots as a function of MW angle (ϕ_{mw}) with particular MW polar angle (θ_{mw}) , as shown in figure 7.2.



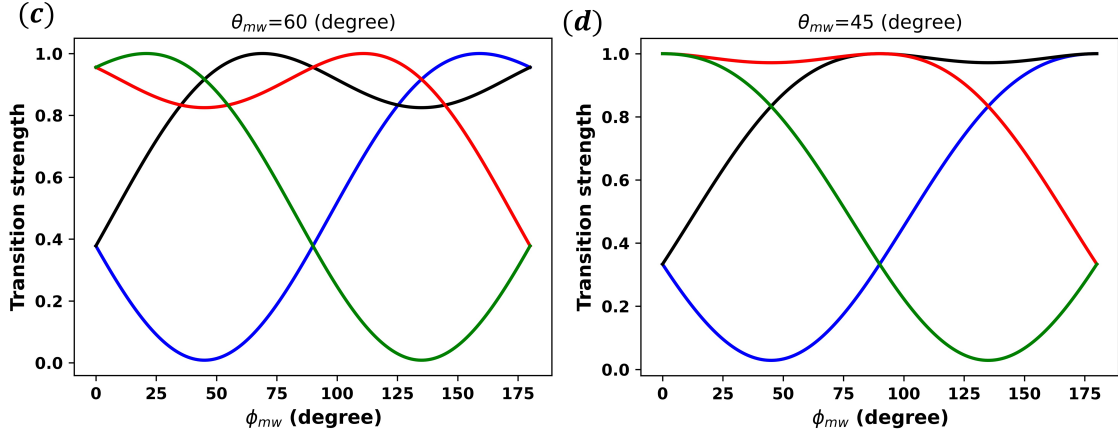


Figure 7.2: The simulation plots show the transition strength as a function of MW angle (ϕ_{mw}) for a particular MW polar angle (θ_{mw}). The plots are colour-coded where the Blue plot represents the transition strength of the NV_1 family, while the Black, Red, and Green plots represent the transition strength of families NV_2 , NV_3 , and NV_4 , respectively. The values of θ_{mw} used for the plots are as follows: (a) $\theta_{mw} = 90^0$, (b) $\theta_{mw} = 80^0$, (c) $\theta_{mw} = 60^0$, and (d) $\theta_{mw} = 45^0$.

The simulation plots 7.2 represent the transition strength as a function of the MW field angle (ϕ_{mw}) for all NV orientations. The two NV orientation NV_1 and NV_3 (and NV_2 and NV_4) makes a pairs for the MW polar angle ($\theta_{mw} = 90^0$) as shown in figure 7.2(a). So we can not determine all four orientations of the NV centers in the ODMR spectrum of the ensemble of NV centers. While we can clearly determine all four orientations of the NV centers by analyzing transition strength for θ_{mw} other than 90^0 degree, as shown in the figures 7.2 (b), (c) and (d). Hence, the study of transition strength with the orientation of the MW field enables us to determine all four orientations of the NV centers. Based on this study, we propose a novel method of vector magnetometry, which is thoroughly described in the following section.

7.2 A novel method for vector magnetometry

One of the distinctive applications of NV center-based quantum sensors is the ability to reconstruct a complete magnetic field vector. Previous research has shown that the magnetic field vector can be determined by utilizing the four orientations of the NV centers in the

ensemble [47, 48]. However, identifying the pair of peaks that correspond to the NV orientation presents a significant challenge in vector magnetometry, as the ODMR spectrum of an NV center ensemble exhibits eight resonance peaks at a finite magnetic field, as depicted in the simulation plot in figure 7.3. To address this issue, we propose a new method that employs MW polarization, which we discuss in detail in this section, based on our theoretical model.

To perform vector magnetometry using MW polarization, we propose the following experimental method:

- First, We obtain the CW ODMR spectrum of the ensemble of NV centers at a finite magnetic field, which displays eight resonance peaks, as shown in figure 7.3.
- We utilize the results of our theoretical model described in section 7.1.2 to identify the pairs of peaks that correspond to the NV orientation. By observing the contrast/transition strength of each peak as the MW field rotates in the lab frame, we obtain experimental data of transition strength as a function of MW angle (ϕ_{mw}).
- Then, we can compare the experimental data with the simulation plots shown in figure 7.2 or fit transition strength equation for each of the four orientation families on the obtained experimental data to identify the pairs of peaks corresponding to the NV orientations.
- To understand the method, let's assume that we identify a pair of peaks (4,5) corresponding to NV_1 orientation using the experimental data of transition strength as MW angle. Similarly, we can identify others the pairs of peaks (1,8), (3,6) and (2,7) correspond to NV_2 , NV_3 and NV_4 orientations, respectively. (see figure 7.3)
- After assigning the peaks to the corresponding NV orientation, we can determine the values of B_1 , B_2 , B_3 and B_4 by measuring the splitting between the pair of peaks in the ODMR spectrum of the ensemble, as depicted in the simulation figure 7.3.
- As the theoretical model suggests, we can take the projection of the lab frame magnetic field vectors on each NV orientation. the analytical expressions of the axial magnetic

field experienced by each NV orientation are given by,

$$B_1 = \frac{1}{\sqrt{3}}(B_X + B_Y + B_Z) \quad (7.2.1a)$$

$$B_2 = \frac{1}{\sqrt{3}}(-B_X + B_Y - B_Z) \quad (7.2.1b)$$

$$B_3 = \frac{1}{\sqrt{3}}(-B_X - B_Y + B_Z) \quad (7.2.1c)$$

$$B_4 = \frac{1}{\sqrt{3}}(B_X - B_Y - B_Z) \quad (7.2.1d)$$

- We can then solve equations 7.2.1 with consideration of the direction of the magnetic field with respect to NV orientation to determine the lab frame magnetic field vector $\mathbf{B} = (B_X, B_Y, B_Z)$. In this way, we are able to perform vector magnetometry using the rotation of the MW polarization.

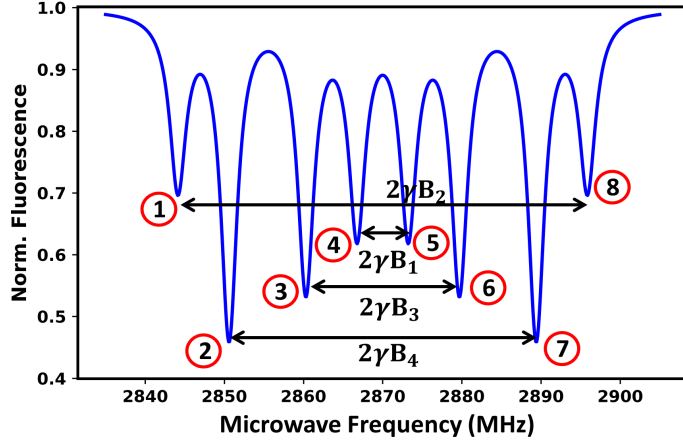


Figure 7.3: Simulation plot of the ODMR spectrum of an ensemble of NV centers in the presence of a finite magnetic field.

Hence, we can reconstruct the magnetic field vector by following the above steps. The transition strength uniquely depends on the MW orientation for each NV orientation in the ensemble. These studies lead us to identify the pair of resonance peaks corresponding to the NV orientations. This information helps us to determine the lab frame magnetic field vector. Vector magnetometry is crucial for the magnetic field imaging experiments such as magnetic field imaging of 2D magnetic material, transistor chips etc. The new method described in this chapter provides a novel approach in the field of vector magnetometry.

Chapter 8

Conclusion and Future Outlook

The interaction between the various environmental fields and the magnetic dipole of electrons of the NV center limits its sensing application. Hence, understanding the behaviour and properties of the NV center under the influence of these environmental fields, like an effective field at zero magnetic field, is essential for advancing quantum technology. Within the scope of this thesis, we investigated the quantum dynamics of the NV center at the zero magnetic field.

8.1 Conclusion

We started this thesis by describing the fundamental properties of the NV center. We discussed the optical properties and spin manipulation in chapter 2, essential to comprehending ODMR spectroscopy. The following chapter discussed the home-built confocal setup and various measurement techniques used in our investigations.

This thesis covered the three different types of investigation on the NV center at zero magnetic field. We thoroughly examined the influence of the intrinsic effective field on the energy levels of the NV center at zero magnetic field. We explored a previously unexplored area, namely the high-effective field regime, which we discuss in detail in our paper [18]. The shifting of the hyperfine spectrum and the splitting between coupled inner states help us determine the magnitude of the intrinsic effective field. Our paper also includes a comprehensive discussion of how the effective field impacts the transition strength when exposed to an arbitrarily polarised microwave (MW) field. Our findings suggest that the transition

imbalance observed in the hyperfine spectrum at zero magnetic field is caused by the relative angle between the MW angle $2\phi_{mw}$ and the azimuthal angle of the effective field ϕ_{Π} .

Further, we demonstrated the selection rule for magnetic dipole transition of the NV center by utilizing the circular polarized MW field in chapter 5. We also introduce the theoretical model that explains the selectivity of the transitions for a particular circular MW field. Our model also suggests that the orientation of the NV center in the laboratory frame can impact the selectivity of spin transitions. Furthermore, we discussed the dark state, which is observable with a circularly polarized MW field, but does not appear in the hyperfine spectrum at zero magnetic field with a linear MW field.

In the following chapter 6, we demonstrated the novel approach to control the transitions between inner states at zero magnetic field using the MW field and RF field simultaneously. We provided a mathematical explanation for this experimental approach, and our results were consistent with the experimental findings. Our observations indicated that the splitting of the inner state is proportional to the magnitude of the applied RF field, which can be used to determine the magnitude of the applied RF field.

Additionally, this thesis also included the study of an ensemble of NV centers to explore vector magnetometry using the MW field. We developed a new theoretical framework to analyze the spin transitions of all four orientations of NV centers in a diamond sample with a (1, 0, 0) orientation, which we discussed in detail in Chapter 7. Our model yielded outcomes indicating that the transition strength of spin states for all four NV orientations is unique and reliant on the MW field's orientation. We also illustrate simulations based on the model's findings, which enabled us to observe the transition strength as a function of the MW field angle (ϕ_{mw}) for specific polar angles (θ_{mw}). Finally, we introduced a novel approach to vector magnetometry that employs the rotation of the MW field and leverages the results of our proposed theoretical model.

8.2 Outlook

The above investigations not only advance our understanding of the NV center but also contribute to the development of new high-sensitive NV center-based quantum sensors. Looking ahead, we suggest an avenue for future research that involves determining the orientation of the effective field by examining the transition imbalance of the inner states in relation to the azimuthal angle of the MW field (ϕ_{mw}). This experiment would be akin to the charge sensing study conducted by Mittiga et al. [52].

Moreover, the novel method for vector magnetometry provides the advances in the field of magnetic field imaging, such as imaging of the magnetic field of 2D magnets, and magnetic field mapping of electronic transistor circuits. The study of MW angle-dependent transition strength or contrast cam helps us to determine a single NV center in the diamond.

Furthermore, the knowledge gained from the thesis can contribute to improving the sensitivity of magnetic field detection. Specifically, the findings on transition strength using an arbitrarily polarized MW field can be utilized to enhance the technology. This can be further advanced by exploring the potential benefits of combining a polarized electric field of the laser beam and a polarized MW field, which can open up new research opportunities in the field of NV center sensitivity enhancement and lead to the development of more advanced versions of quantum sensing technology.

Appendix A

Spin-1 System

As discussed in Chapter 2, NV center has a spin-1 system as a result of having two unpaired electrons. To comprehend the behavior of NV center, one needs to have a comprehensive understanding of the mathematics behind spin-1 systems. This appendix provides a detailed explanation of the mathematical expressions related to spin-1 systems and also includes the derivation of Eigenenergies and Eigenstates of the ground state Hamiltonian of NV center, which were discussed in Section 2.3.

A.1 Matrices for Spin-1 System

Spin vectors are usually represented in terms of their Hermitian Cartesian component operators as $\hat{\mathbf{S}} = (\hat{S}_x, \hat{S}_y, \hat{S}_z)$. where,

$$\hat{S}_x = \frac{1}{\sqrt{2}} \begin{pmatrix} 0 & 1 & 0 \\ 1 & 0 & 1 \\ 0 & 1 & 0 \end{pmatrix} \quad \hat{S}_y = \frac{1}{\sqrt{2}} \begin{pmatrix} 0 & -i & 0 \\ i & 0 & -i \\ 0 & i & 0 \end{pmatrix} \quad \hat{S}_z = \begin{pmatrix} 1 & 0 & 0 \\ 0 & 0 & 0 \\ 0 & 0 & -1 \end{pmatrix}$$

A.2 Ground state Hamiltonian of NV center

The NV axis is regarded as a reference axis for quantization, and the ground triplet states are described by the eigenvectors of the \hat{S}_z operator. Hence, It has three eigenstates, denoted as $|0\rangle$, $|-\rangle$ and $|+\rangle$ in the m_s basis. To determine the energy levels of the NV center for a given Hamiltonian, the following approach can be used:

The Hamiltonian of NV center with external magnetic field is given by,

$$\hat{H}_0 = D\hat{S}_z^2 + \gamma B_z \hat{S}_z \quad (\text{A.2.1})$$

Solving Hamiltonian A.2.1, we get eigenenergies and eigen state of NV center in presence of external magnetic field,

$$E_{|+1\rangle} = D + \gamma B_z, \quad (\text{A.2.2a})$$

$$E_{|-1\rangle} = D - \gamma B_z, \quad (\text{A.2.2b})$$

The Hamiltonian of the NV center's ground state can be modified to include the hyperfine interaction originating from the nuclear spin of ^{14}N .

$$\hat{H} = D\hat{S}_z^2 + \gamma B_z \hat{S}_z + A_{HF} \hat{S}_z \hat{I}_z \quad (\text{A.2.3})$$

The nuclear spin operator $\hat{\mathbf{I}} = (\hat{I}_x, \hat{I}_y, \hat{I}_z)$ is also a spin-1 for the ^{14}N atom. To describe the interaction between the nuclear spin and the electron spins of the NV center, a tensor product is utilized. As a result, the hyperfine eigenstates of the NV center are expressed in the $|m_s, m_I\rangle$ basis. The eigenenergies of Hamiltonian A.2.3 are,

$$E_{|+1,+1\rangle} = D + \gamma B_z + A_{HF}, \quad (\text{A.2.4a})$$

$$E_{|+1,0\rangle} = D + \gamma B_z, \quad (\text{A.2.4b})$$

$$E_{|+1,-1\rangle} = D + \gamma B_z - A_{HF}, \quad (\text{A.2.4c})$$

$$E_{|-1,-1\rangle} = D - \gamma B_z + A_{HF}, \quad (\text{A.2.4d})$$

$$E_{|-1,0\rangle} = D - \gamma B_z, \quad (\text{A.2.4e})$$

$$E_{|-1,+1\rangle} = D - \gamma B_z - A_{HF}, \quad (\text{A.2.4f})$$

The subscripts in the above equations indicate the respective eigenstate for that particular energy. equations A.2.2 and A.2.4 were employed to illustrate the energy level diagram of the NV center's ground state in figure 2.2(a).

A.3 Hamiltonian of an NV center at zero magnetic field

Chapter 4 reported the Hamiltonian of an NV center with a high effective field ($\Pi_{\perp} \geq |A_{HF}|$) at zero magnetic field. In this section, we described the Hamiltonian of an NV center at zero magnetic field with low effective field regime ($\Pi_{\perp} \ll |A_{HF}|$). Hence, The Hamiltonian $\hat{\mathcal{H}}$ of the NV center in the presence of the intrinsic effective field and the axial hyperfine field can be expressed as,

$$\hat{\mathcal{H}} = D\hat{S}_z^2 + A_{HF}\hat{S}_z\hat{I}_z + \Pi_{\parallel}\hat{S}_z^2 + \Pi_x(\hat{S}_x^2 - \hat{S}_y^2) + \Pi_y(\hat{S}_x\hat{S}_y + \hat{S}_y\hat{S}_x) \quad (\text{A.3.1})$$

Where all symbols have their usual meaning described in section 4.1. Eigenenergies of this Hamiltonian with low effective field regime can be expressed as,

$$E_{|-,0\rangle} = D + \Pi_{\parallel} - \Pi_{\perp}, \quad (\text{A.3.2a})$$

$$E_{|+,0\rangle} = D + \Pi_{\parallel} + \Pi_{\perp}, \quad (\text{A.3.2b})$$

$$E_{|+1,+1\rangle} = D + \Pi_{\parallel} - |A_{HF}|, \quad (\text{A.3.2c})$$

$$E_{|-1,+1\rangle} = D + \Pi_{\parallel} + |A_{HF}|, \quad (\text{A.3.2d})$$

$$E_{|-1,-1\rangle} = D + \Pi_{\parallel} - |A_{HF}|, \quad (\text{A.3.2e})$$

$$E_{|+1,-1\rangle} = D + \Pi_{\parallel} + |A_{HF}|, \quad (\text{A.3.2f})$$

Since, The transverse component of effective field Π_{\perp} cause to coupled the states $|\pm 1, 0\rangle$ with each other, which can be described by,

$$|-,0\rangle = |-\rangle_0 \otimes |0\rangle = \frac{1}{\sqrt{2}}(|+1\rangle - e^{i\phi_{\Pi}}|-1\rangle) \otimes |0\rangle, \quad (\text{A.3.3a})$$

$$|+,0\rangle = |+\rangle_0 \otimes |0\rangle = \frac{1}{\sqrt{2}}(|+1\rangle + e^{i\phi_{\Pi}}|-1\rangle) \otimes |0\rangle, \quad (\text{A.3.3b})$$

Additionally, The hyperfine coupling parameter (A_{HF}) limit the influence of the effective field on the $|\pm 1, \pm 1\rangle$ and $|\pm 1, \mp 1\rangle$. We depict energy-level diagram in figure 4.1 based on equations A.3.2.

Appendix B

Time-Dependent Hamiltonian in Interaction Picture

When an oscillating magnetic field is applied to the NV center, it creates a time-varying perturbation in its ground state Hamiltonian. The interaction between the magnetic dipole of the NV center and the MW field causes changes in the spin state of the system. To calculate the transition probability of these spin state transitions, the Interaction picture can be employed in the calculations. This Appendix provides a detailed explanation of the mathematical approach for determining the transition strength (or probability) using the Interaction picture and the rotating wave approximation (RWA).

B.1 Derivation of rotating frame Hamiltonian for the linear MW field

Prior to analyzing the Hamiltonian with a general MW field polarization, we will first examine the case of simple linear polarization of MW fields. Let's consider the oscillating magnetic field with ω_{mw} angular frequency applying to the x-axis of the NV coordinate system as $\mathbf{B}(t) = B_{mw} \cos(\omega_{mw}t) \hat{\mathbf{e}}_x$. This field drive the spin states from $|0\rangle$ to $|+1\rangle$ (and $| -1\rangle$) at its resonance frequency. The time-dependent Hamiltonian can be expressed as,

$$\hat{H}_{mw}(t) = \gamma \mathbf{B}(t) \cdot \hat{\mathbf{S}} = \gamma B_{mw} \cos(\omega_{mw}t) \hat{S}_x \quad (\text{B.1.1})$$

Hence, we can write total Hamiltonian from equations A.2.1 and B.1.1,

$$\hat{H}(t) = \hat{H}_0 + \hat{H}_{mw}(t) = D\hat{S}_z^2 + \gamma B_z \hat{S}_z + \gamma B_{mw} \cos(\omega_{mw} t) \hat{S}_x \quad (\text{B.1.2})$$

Now, we convert the above equation into a time-independent Hamiltonian in the interaction picture using the following mathematical operations.

$$\begin{aligned} \hat{H}_{mw}(t) &= (\gamma B_{mw}) \cos(\omega_{mw} t) \hat{S}_x \\ &= (\gamma B_{mw}) \left[[\cos(\omega t) \hat{S}_x + \sin(\omega t) \hat{S}_y] + [\cos(\omega t) \hat{S}_x - \sin(\omega t) \hat{S}_y] \right] \\ &= (\gamma B_{mw}) \left[\frac{e^{i\omega t} + e^{-i\omega t}}{2} \hat{S}_x + \frac{e^{i\omega t} - e^{-i\omega t}}{2i} \hat{S}_y \right] + \left[\frac{e^{i\omega t} + e^{-i\omega t}}{2} \hat{S}_x - \frac{e^{i\omega t} - e^{-i\omega t}}{2i} \hat{S}_y \right] \\ &= (\gamma B_{mw}) \left[\left[e^{i\omega t} \left(\frac{\hat{S}_x - i\hat{S}_y}{2} \right) + e^{-i\omega t} \left(\frac{\hat{S}_x + i\hat{S}_y}{2} \right) \right] + \left[e^{i\omega t} \left(\frac{\hat{S}_x + i\hat{S}_y}{2} \right) + e^{-i\omega t} \left(\frac{\hat{S}_x - i\hat{S}_y}{2} \right) \right] \right] \\ &= (\gamma B_{mw}) \left[[e^{i\omega t} \hat{S}_- + e^{-i\omega t} \hat{S}_+] + [e^{i\omega t} \hat{S}_+ + e^{-i\omega t} \hat{S}_-] \right] \end{aligned} \quad (\text{B.1.3})$$

We can determine the rotating frame Hamiltonian (\hat{H}_I) by operating below equation on the total Hamiltonian equation B.1.2,

$$\hat{H}_I = i \frac{d\hat{U}^\dagger}{dt} \hat{U} + \hat{U}^\dagger \hat{H}(t) \hat{U} \quad (\text{B.1.4})$$

The unitary operator as $\hat{U} = \exp(-i \omega_{mw} t \hat{S}_z^2)$ is utilize for further calculations.

$$\hat{H}_I = -\omega_{mw} \hat{S}_z^2 + \hat{U}^\dagger (\hat{H}_0 + \hat{H}_{mw}(t)) \hat{U}$$

Since, \hat{H}_0 is commute with \hat{S}_z^2 implies $\hat{U}^\dagger \hat{H}_0 \hat{U} = \hat{H}_0$. While calculation for $\hat{U}^\dagger \hat{H}_{mw}(t) \hat{U}$ is given below,

$$\hat{U}^\dagger \hat{H}_{mw}(t) \hat{U} = (\gamma B_{mw}) \left[[e^{i\omega t} \hat{U}_0^\dagger \hat{S}_- \hat{U}_0 + e^{-i\omega t} \hat{U}_0^\dagger \hat{S}_+ \hat{U}_0] + [e^{i\omega t} \hat{U}_0^\dagger \hat{S}_+ \hat{U}_0 + e^{-i\omega t} \hat{U}_0^\dagger \hat{S}_- \hat{U}_0] \right] \quad (\text{B.1.5})$$

To solve this further, we make use of the quantum mechanics formula, which is expressed as follows.

$$e^{xA} B e^{-xA} = B + [A, B]x + [A, [A, B]] \frac{x^2}{2!} + [A, [A, [A, B]]] \frac{x^3}{3!} + \dots \quad (\text{B.1.6})$$

Using above formula,

$$\hat{U}^\dagger \hat{S}_+ \hat{U} = e^{i\omega t \hat{S}_z^2} \hat{S}_+ e^{-i\omega t \hat{S}_z^2} = \frac{1}{\sqrt{2}} \begin{pmatrix} 0 & e^{i\omega t} & 0 \\ 0 & 0 & e^{-i\omega t} \\ 0 & 0 & 0 \end{pmatrix} \quad (\text{B.1.7})$$

$$\hat{U}^\dagger \hat{S}_- \hat{U} = e^{i\omega t \hat{S}_z^2} \hat{S}_- e^{-i\omega t \hat{S}_z^2} = \frac{1}{\sqrt{2}} \begin{pmatrix} 0 & 0 & 0 \\ e^{-i\omega t} & 0 & 0 \\ 0 & e^{i\omega t} & 0 \end{pmatrix} \quad (\text{B.1.8})$$

Using equations B.1.7 and B.1.8, We can rewrite the equation B.1.5 as follows,

$$\hat{U}^\dagger \hat{H}_{mw}(t) \hat{U} = \frac{\gamma B_{mw}}{\sqrt{2}} \begin{pmatrix} 0 & 1 + e^{2i\omega t} & 0 \\ 1 + e^{-2i\omega t} & 0 & e^{-2i\omega t} + 1 \\ 0 & e^{2i\omega t} + 1 & 0 \end{pmatrix} \quad (\text{B.1.9})$$

We neglect rapidly oscillating terms under rotating wave approximation (RWA) [53],

$$\hat{U}^\dagger \hat{H}_{mw}(t) \hat{U} = \frac{\gamma B_{mw}}{\sqrt{2}} \begin{pmatrix} 0 & 1 & 0 \\ 1 & 0 & 1 \\ 0 & 1 & 0 \end{pmatrix} = \gamma B_{mw} \hat{S}_x \quad (\text{B.1.10})$$

Therefore, the total Hamiltonian can be expressed in the rotating frame or interaction picture as follows,

$$\hat{H}_I = D' \hat{S}_z^2 + \gamma B_z \hat{S}_z + \gamma B_{mw} \hat{S}_x \quad (\text{B.1.11})$$

Similarly, the Hamiltonian in the rotating frame with a microwave (MW) field aligned along the y-axis of the NV coordinate can be obtained using the following expression,

$$\hat{H}_I = D' \hat{S}_z^2 + \gamma B_z \hat{S}_z + \frac{\gamma B_{mw}}{\sqrt{2}} \begin{pmatrix} 0 & 1 & 0 \\ 1 & 0 & -1 \\ 0 & -1 & 0 \end{pmatrix} \quad (\text{B.1.12})$$

In the next section, we work on the interaction Hamiltonian for the general MW polarization field based on calculations of this section.

B.2 Rotating frame Hamiltonian for arbitrary polarized MW field

The most general expression for the microwave field vector $\mathbf{B}(t)$ perpendicular to the NV symmetry axis can be written using the parameters ϕ_{mw} and ϵ_{mw} as [54]

$$\begin{aligned}\mathbf{B}(t) = & B_{mw} [\cos \epsilon_{mw} (\cos \phi_{mw} \mathbf{e}_x + \sin \phi_{mw} \mathbf{e}_y) \cos \omega t \\ & + \sin \epsilon_{mw} (-\sin \phi_{mw} \mathbf{e}_x + \cos \phi_{mw} \mathbf{e}_y) \sin \omega t]\end{aligned}\quad (\text{B.2.1})$$

where the parameter $\epsilon_{mw} = \pm \arctan \left(\frac{b}{a} \right)$ is known as the ellipticity angle. The time evolution of the magnetic field vector traces out an ellipse in the xy plane with a and b being the length of the semi-major and semi-minor axes of the ellipse, and the parameter ϕ_{mw} is the angle the major axis of the ellipse makes with the x -axis. By introducing the parameter λ_{mw} , we can also parameterize the microwave magnetic field $\mathbf{B}(t)$ in terms of the ratio of the amplitudes of the left-circularly polarized microwaves (σ^+) and the right-circularly polarized microwaves (σ^-) as

$$\begin{aligned}\mathbf{B}(t) = & \mathbf{B}_{mw,\sigma^+}(t) + \mathbf{B}_{mw,\sigma^-}(t) \\ = & \cos \left(\frac{\pi}{4} - \epsilon_{mw} \right) \left(\frac{B_{mw}}{\sqrt{2}} [\cos(\omega t + \phi_{mw}) \mathbf{e}_x + \sin(\omega t + \phi_{mw}) \mathbf{e}_y] \right. \\ & \left. + \lambda_{mw} \frac{B_{mw}}{\sqrt{2}} [\cos(\omega t - \phi_{mw}) \mathbf{e}_x - \sin(\omega t - \phi_{mw}) \mathbf{e}_y] \right)\end{aligned}$$

where the parameter λ_{mw} is related to ϵ_{mw} by $\lambda_{mw} = \tan \left(\frac{\pi}{4} - \epsilon_{mw} \right)$. From equation B.1.1, The Hamiltonian for an arbitrary polarized MW field can be expressed as,

$$\begin{aligned}\hat{H}_{mw}(t) = & \gamma (\mathbf{B}_{mw,\sigma^+}(t) + \mathbf{B}_{mw,\sigma^-}(t)) \cdot \hat{\mathbf{S}} \\ = & \cos \left(\frac{\pi}{4} - \epsilon_{mw} \right) \left(\frac{\Omega}{\sqrt{2}} [\cos(\omega t + \phi_{mw}) \hat{S}_x + \sin(\omega t + \phi_{mw}) \hat{S}_y] \right. \\ & \left. + \lambda_{mw} \frac{\Omega}{\sqrt{2}} [\cos(\omega t - \phi_{mw}) \hat{S}_x - \sin(\omega t - \phi_{mw}) \hat{S}_y] \right)\end{aligned}$$

where $\Omega = \gamma B_{mw}$ is the Rabi frequency and ω is the frequency of the microwave. The matrix representation for the Hamiltonian in the basis $\{|+1\rangle, |0\rangle, |-1\rangle\}$ is given by

$$\hat{H}_{mw}(t) = \cos\left(\frac{\pi}{4} - \epsilon_{mw}\right) \frac{\Omega}{2} \begin{bmatrix} 0 & e^{-i(\omega t + \phi_{mw})} & 0 \\ e^{i(\omega t + \phi_{mw})} & 0 & e^{-i(\omega t + \phi_{mw})} \\ 0 & e^{i(\omega t + \phi_{mw})} & 0 \end{bmatrix} + \cos\left(\frac{\pi}{4} - \epsilon_{mw}\right) \frac{\Omega}{2} \begin{bmatrix} 0 & \lambda_{mw} e^{i(\omega t - \phi_{mw})} & 0 \\ \lambda_{mw} e^{-i(\omega t - \phi_{mw})} & 0 & \lambda_{mw} e^{i(\omega t - \phi_{mw})} \\ 0 & \lambda_{mw} e^{-i(\omega t - \phi_{mw})} & 0 \end{bmatrix} \quad (\text{B.2.2})$$

where we used the relation $\lambda_{mw} = \tan\left(\frac{\pi}{4} - \epsilon_{mw}\right)$. Neglecting all the time-dependent terms rotating at 2ω under rotating wave approximation,

$$\begin{aligned} \hat{H}_I^{mw} &= \frac{\Omega}{2} \begin{bmatrix} 0 & \cos\left(\frac{\pi}{4} - \epsilon_{mw}\right) e^{-i\phi_{mw}} & 0 \\ \cos\left(\frac{\pi}{4} - \epsilon_{mw}\right) e^{i\phi_{mw}} & 0 & \sin\left(\frac{\pi}{4} - \epsilon_{mw}\right) e^{-i\phi_{mw}} \\ 0 & \sin\left(\frac{\pi}{4} - \epsilon_{mw}\right) e^{i\phi_{mw}} & 0 \end{bmatrix} \\ &= \frac{\Omega}{2} \left[\cos\left(\frac{\pi}{4} - \epsilon_{mw}\right) e^{-i\phi_{mw}} |1\rangle \langle 0| + \sin\left(\frac{\pi}{4} - \epsilon_{mw}\right) e^{i\phi_{mw}} |-1\rangle \langle 0| \right] \\ &\quad + \frac{\Omega}{2} \left[\sin\left(\frac{\pi}{4} - \epsilon_{mw}\right) e^{-i\phi_{mw}} |0\rangle \langle -1| + \cos\left(\frac{\pi}{4} - \epsilon_{mw}\right) e^{i\phi_{mw}} |0\rangle \langle 1| \right] \\ &= \frac{\Omega}{2} \left[\cos\left(\frac{\pi}{4} - \epsilon_{mw}\right) e^{-i\phi_{mw}} |1\rangle + \sin\left(\frac{\pi}{4} - \epsilon_{mw}\right) e^{i\phi_{mw}} |-1\rangle \right] \langle 0| + \text{H.c.} \quad (\text{B.2.3}) \end{aligned}$$

where H.c. is the Hermitian conjugate.

Bibliography

- [1] Andrew Steane. “Quantum computing.” In: *Reports on Progress in Physics*, **64** 117 (1998).
- [2] Nicolas Gisin, Grégoire Ribordy, Wolfgang Tittel, and Hugo Zbinden. “Quantum cryptography.” In: *Reviews of Modern Physics*, **74** 145195 (2002).
- [3] C. L. Degen, F. Reinhard, and P. Cappellaro. “Quantum sensing.” In: *Reviews of Modern Physics*, **89** 035002 (2017).
- [4] Romana Schirhagl, Kevin Chang, Michael Loretz, and Christian L. Degen. “Nitrogen-Vacancy Centers in Diamond: Nanoscale Sensors for Physics and Biology.” In: *Annual Review of Physical Chemistry*, **65** 83105 (2014).
- [5] J. R. Maze et al. “Nanoscale magnetic sensing with an individual electronic spin in diamond.” In: *Nature*, **455** 644647 (2008).
- [6] F. Dolde et al. “Electric-field sensing using single diamond spins.” In: *Nature Physics*, **7** 459463 (2011).
- [7] Michael S. J. Barson et al. “Nanomechanical Sensing Using Spins in Diamond.” In: *Nano Letters*, **17** 14961503 (2017).
- [8] Gopalakrishnan Balasubramanian, Philipp Neumann, Daniel Twitchen, Fedor Jelezko, and Jörg Wrachtrup. “Ultralong spin coherence time in isotopically engineered diamond.” In: *Nature Materials*, **8** 383387 (2009).
- [9] A. Gruber, A. Dräbenstedt, C. Tietz, L. Fleury, J. Wrachtrup, and C. von Borczyskowski. “Scanning Confocal Optical Microscopy and Magnetic Resonance on Single Defect Centers.” In: *Science*, **276** 20122014 (1997).

- [10] Hunter C. Davis, Pradeep Ramesh, Aadyot Bhatnagar, Audrey Lee-Gosselin, John F. Barry, David R. Glenn, Ronald L. Walsworth, and Mikhail G. Shapiro. “Mapping the microscale origins of magnetic resonance image contrast with subcellular diamond magnetometry.” In: *Nature Communications*, **9** 131 (2018).
- [11] D. Le Sage et al. “Optical magnetic imaging of living cells.” In: *Nature*, **496** 486489 (2013).
- [12] D. R. Glenn, R. R. Fu, P. Kehayias, D. Le Sage, E. A. Lima, B. P. Weiss, and R. L. Walsworth. “Micrometer-scale magnetic imaging of geological samples using a quantum diamond microscope.” In: *Geochemistry, Geophysics, Geosystems*, **18** 32543267 (2017).
- [13] Scott E. Lillie, David A. Broadway, Nikolai Dotschuk, Ali Zavabeti, David A. Simpson, Tokuyuki Teraji, Torben Daeneke, Lloyd C. L. Hollenberg, and Jean-Philippe Tetienne. “Magnetic noise from ultrathin abrasively deposited materials on diamond.” In: *Physical Review Materials*, **2** 116002 (2018).
- [14] David A. Simpson, Jean-Philippe Tetienne, Julia M. McCoey, Kumaravelu Ganeshan, Liam T. Hall, Steven Petrou, Robert E. Scholten, and Lloyd C. L. Hollenberg. “Magneto-optical imaging of thin magnetic films using spins in diamond.” In: *Scientific Reports*, **6** 22797 (2016).
- [15] Francesco Casola, Toeno van der Sar, and Amir Yacoby. “Probing condensed matter physics with magnetometry based on nitrogen-vacancy centres in diamond.” In: *Nature Reviews Materials*, **3** 17088 (2018).
- [16] Lilian Childress and Ronald Hanson. “Diamond NV centers for quantum computing and quantum networks.” In: *MRS Bulletin*, **38** 134138 (2013).
- [17] Sébastien Pezzagna and Jan Meijer. “Quantum computer based on color centers in diamond.” In: *Applied Physics Reviews*, **8** 011308 (2021).
- [18] Shashank Kumar, Pralekh Dubey, Sudhan Bhadade, Jemish Naliyapara, Jayita Saha, and Phani Peddibhotla. “High-resolution spectroscopy of a single nitrogen-vacancy defect at zero magnetic field.” In: *Quantum Science and Technology*, **8** 025011 (2023).

- [19] Cui Jin-Ming, Chen Xiang-Dong, Fan Le-Le, Gong Zhao-Jun, Zou Chong-Wen, Sun Fang-Wen, Han Zheng-Fu, and Guo Guang-Can. “Generation of Nitrogen-Vacancy Centers in Diamond with Ion Implantation.” In: *Chinese Physics Letters*, **29** 036103 (2012).
- [20] Yafei Zhang, Chuanyi Zang, Hongan Ma, Zhongzhu Liang, Lin Zhou, Shangsheng Li, and Xiaopeng Jia. “HPHT synthesis of large single crystal diamond doped with high nitrogen concentration.” In: *Diamond and Related Materials*, **17** 209211 (2008).
- [21] Michael Schwander and Knut Partes. “A review of diamond synthesis by CVD processes.” In: *Diamond and Related Materials*, **20** 12871301 (2011).
- [22] Yoshimi Mita. “Change of absorption spectra in type-Ib diamond with heavy neutron irradiation.” In: *Physical Review B*, **53** 1136064 (1996).
- [23] B. Campbell and A. Mainwood. “Radiation Damage of Diamond by Electron and Gamma Irradiation.” In: *physica status solidi (a)*, **181** 99107 (2000).
- [24] Marcus W. Doherty, Neil B. Manson, Paul Delaney, Fedor Jelezko, Jörg Wrachtrup, and Lloyd C.L. Hollenberg. “The nitrogen-vacancy colour centre in diamond.” In: *Physics Reports*, **528** 145 (2013).
- [25] J H N Loubser and J A van Wyk. “Electron spin resonance in the study of diamond.” In: *Reports on Progress in Physics*, **41** 1201 (1978).
- [26] A. Lenef and S. C. Rand. “Electronic structure of the N-V center in diamond: Theory.” In: *Physical Review B*, **53** 1344113455 (1996).
- [27] Adam Gali, Maria Fyta, and Efthimios Kaxiras. “Ab initio supercell calculations on nitrogen-vacancy center in diamond: Electronic structure and hyperfine tensors.” In: *Physical Review B*, **77** 155206 (2008).
- [28] L Rondin, J-P Tetienne, T Hingant, J-F Roch, P Maletinsky, and V Jacques. “Magnetometry with nitrogen-vacancy defects in diamond.” In: *Reports on Progress in Physics*, **77** 056503 (2014).

- [29] A T Collins, M F Thomaz, and M I B Jorge. “Luminescence decay time of the 1.945 eV centre in type Ib diamond.” In: *Journal of Physics C: Solid State Physics*, **16** 2177 (1983).
- [30] Zhi-Hui Wang and Susumu Takahashi. “Spin decoherence and electron spin bath noise of a nitrogen-vacancy center in diamond.” In: *Physical Review B*, **87** 115122 (2013).
- [31] James L. Webb, Joshua D. Clement, Luca Troise, Sepehr Ahmadi, Gustav Juhl Johansen, Alexander Huck, and Ulrik L. Andersen. “Nanotesla sensitivity magnetic field sensing using a compact diamond nitrogen-vacancy magnetometer.” In: *Applied Physics Letters*, **114** 231103 (2019).
- [32] A. Dréau, M. Lesik, L. Rondin, P. Spinicelli, O. Arcizet, J.-F. Roch, and V. Jacques. “Avoiding power broadening in optically detected magnetic resonance of single NV defects for enhanced dc magnetic field sensitivity.” In: *Physical Review B*, **84** 195204 (2011).
- [33] Ning Wang et al. “Zero-field magnetometry using hyperfine-biased nitrogen-vacancy centers near diamond surfaces.” In: *Physical Review Research*, **4** 013098 (2022).
- [34] Philipp J. Vetter et al. “Zero- and Low-Field Sensing with Nitrogen-Vacancy Centers.” In: *Physical Review Applied*, **17** 044028 (2022).
- [35] K. D. Jahnke, B. Naydenov, T. Teraji, S. Koizumi, T. Umeda, J. Isoya, and F. Jelezko. “Long coherence time of spin qubits in 12C enriched polycrystalline chemical vapor deposition diamond.” In: *Applied Physics Letters*, **101** 012405 101 (2012).
- [36] Matthew E Trusheim and Dirk Englund. “Wide-field strain imaging with preferentially aligned nitrogen-vacancy centers in polycrystalline diamond.” In: *New Journal of Physics*, **18** 123023 (2016).
- [37] Eric Bersin, Michael Walsh, Sara L. Mouradian, Matthew E. Trusheim, Tim Schröder, and Dirk Englund. “Individual control and readout of qubits in a sub-diffraction volume.” In: *NPJ Quantum Information*, **5** 38 (2019).

- [38] J Kölbl, M Kasperczyk, B Bürgler, A Barfuss, and P Maletinsky. “Determination of intrinsic effective fields and microwave polarizations by high-resolution spectroscopy of single nitrogen-vacancy center spins.” In: *New Journal of Physics*, **21** 113039 (2019).
- [39] Yuhei Sekiguchi, Yusuke Komura, Shota Mishima, Touda Tanaka, Naeko Niikura, and Hideo Kosaka. “Geometric spin echo under zero field.” In: *Nature Communications*, **7** 11668 (2016).
- [40] Thiago P. Mayer Alegre, Charles Santori, Gilberto Medeiros-Ribeiro, and Raymond G. Beausoleil. “Polarization-selective excitation of nitrogen vacancy centers in diamond.” In: *Physical Review B*, **76** 165205 (2007).
- [41] M. Mrózek, J. Mlynarczyk, D. S. Rudnicki, and W. Gawlik. “Circularly polarized microwaves for magnetic resonance study in the GHz range: Application to nitrogen-vacancy in diamonds.” In: *Applied Physics Letters*, **107** 013505 (2015).
- [42] Tatsuma Yamaguchi, Yuichiro Matsuzaki, Soya Saijo, Hideyuki Watanabe, Norikazu Mizuochi, and Junko Ishi-Hayase. “Control of all the transitions between ground state manifolds of nitrogen vacancy centers in diamonds by applying external magnetic driving fields.” In: *Japanese Journal of Applied Physics*, **59** 110907 (2020).
- [43] F. Jelezko, T. Gaebel, I. Popa, A. Gruber, and J. Wrachtrup. “Observation of Coherent Oscillations in a Single Electron Spin.” In: *Physical Review Letters*, **92** 076401 (2004).
- [44] E. R. MacQuarrie, T. A. Gosavi, N. R. Jungwirth, S. A. Bhave, and G. D. Fuchs. “Mechanical Spin Control of Nitrogen-Vacancy Centers in Diamond.” In: *Physical Review Letters*, **111** 227602 (2013).
- [45] P. V. Klimov, A. L. Falk, B. B. Buckley, and D. D. Awschalom. “Electrically Driven Spin Resonance in Silicon Carbide Color Centers.” In: *Physical Review Letters*, **112** 087601 (2014).
- [46] Soya Saijo, Yuichiro Matsuzaki, Shiro Saito, Tatsuma Yamaguchi, Ikuya Hanano, Hideyuki Watanabe, Norikazu Mizuochi, and Junko Ishi-Hayase. “AC magnetic field sensing using continuous-wave optically detected magnetic resonance of nitrogen-vacancy centers in diamond.” In: *Applied Physics Letters*, **113** 082405 (2018).

- [47] F. Münzhuber, F. Bayer, V. Marković, J. Brehm, J. Kleinlein, L. W. Molenkamp, and T. Kiessling. “Polarization-Assisted Vector Magnetometry with No Bias Field Using an Ensemble of Nitrogen-Vacancy Centers in Diamond.” In: *Physical Review Applied*, **14** 014055 (2020).
- [48] Mayeul Chipaux, Alexandre Tallaire, Jocelyn Achard, Sébastien Pezzagna, Jan Meijer, Vincent Jacques, Jean-François Roch, and Thierry Debuisschert. “Magnetic imaging with an ensemble of nitrogen-vacancy centers in diamond.” In: *The European Physical Journal D*, **69** 166 (2015).
- [49] Yusef Maleki and Aleksei M. Zheltikov. “Witnessing quantum entanglement in ensembles of nitrogen vacancy centers coupled to a superconducting resonator.” In: *Optics Express*, **26** 1784917858 (2018).
- [50] L M Pham et al. “Magnetic field imaging with nitrogen-vacancy ensembles.” In: *New Journal of Physics*, **13** 045021 (2011).
- [51] Romana Schirhagl, Kevin Chang, Michael Loretz, and Christian L. Degen. “Nitrogen-Vacancy Centers in Diamond: Nanoscale Sensors for Physics and Biology.” In: *Annual Review of Physical Chemistry*, **65** 83105 (2014).
- [52] T. Mittiga et al. “Imaging the Local Charge Environment of Nitrogen-Vacancy Centers in Diamond.” In: *Physical Review Letters*, **121** 246402 (2018).
- [53] Ying Wu and Xiaoxue Yang. “Strong-Coupling Theory of Periodically Driven Two-Level Systems.” In: *Physical Review Letter*, **98** 013604 (2007).
- [54] M. Auzinsh, D. Budker, and S. Rochester. *Optically Polarized Atoms: Understanding Light-Atom Interactions*. Oxford University Press, 2010. ISBN: 978-0-19-956512-2.